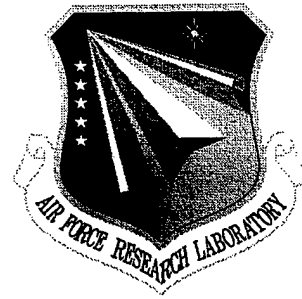


AFRL-IF-RS-TR-1998-174
Final Technical Report
August 1998



**ELECTROMAGNETIC FIELD ANALYSIS OF
DIGITAL CIRCUITS AND MODULES FOR
ELECTROMAGNETIC COMPATIBILITY AND
RELIABILITY**

Northwestern University

Allen Taflove

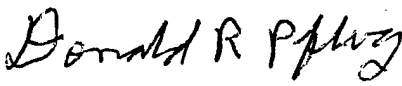
APPROVED FOR PUBLIC RELEASE; DISTRIBUTION UNLIMITED.

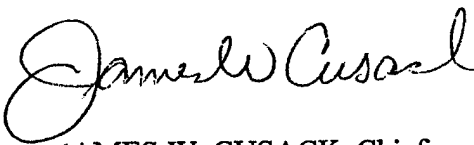
19980929 127

**AIR FORCE RESEARCH LABORATORY
INFORMATION DIRECTORATE
ROME RESEARCH SITE
ROME, NEW YORK**

DIC QUALITY INSPECTED 3

AFRL-IF-RS-TR-1998-174 has been reviewed and is approved for publication.

APPROVED: 
DONALD R. PFLUG
Project Engineer

FOR THE DIRECTOR: 
JAMES W. CUSACK, Chief
Information Systems Division
Information Directorate

DESTRUCTION NOTICE - For classified documents, follow the procedures in DOD 5200.22M, Industrial Security Manual or DOD 5200.1-R, Information Security Program Regulation. For unclassified limited documents, destroy by any method that will prevent disclosure of contents or reconstruction of the document.

If your address has changed or if you wish to be removed from the Air Force Research Laboratory Rome Research Site mailing list, or if the addressee is no longer employed by your organization, please notify Air Force Research Laboratory/IFSB, 525 Brooks Road, Rome, NY 13441-4505. This will assist us in maintaining a current mailing list.

Do not return copies of this report unless contractual obligations or notices on a specific document require that it be returned.

REPORT DOCUMENTATION PAGE			Form Approved OMB No. 0704-0188	
<small>Public reporting burden for this collection of information is estimated to average 1 hour per response, including the time for reviewing instructions, searching existing data sources, gathering and maintaining the data needed, and completing and reviewing the collection of information. Send comments regarding this burden estimate or any other aspect of this collection of information, including suggestions for reducing this burden, to Washington Headquarters Services, Directorate for Information Operations and Reports, 1215 Jefferson Davis Highway, Suite 1204, Arlington, VA 22202-4302, and to the Office of Management and Budget, Paperwork Reduction Project (0704-0188), Washington, DC 20503.</small>				
1. AGENCY USE ONLY (Leave blank)	2. REPORT DATE August 1998	3. REPORT TYPE AND DATES COVERED Final May 95 - Jan 96		
4. TITLE AND SUBTITLE ELECTROMAGNETIC FIELD ANALYSIS OF DIGITAL CIRCUITS AND MODULES FOR ELECTROMAGNETIC COMPATIBILITY AND RELIABILITY		5. FUNDING NUMBERS C - F30602-95-C-0073 PE - 62702F PR - 2338 TA - 03 WU - P9		
6. AUTHOR(S) Allen Taflove		8. PERFORMING ORGANIZATION REPORT NUMBER N/A		
7. PERFORMING ORGANIZATION NAME(S) AND ADDRESS(ES) Northwestern University 633 Clark Street Evanston IL 60208-1110		10. SPONSORING/MONITORING AGENCY REPORT NUMBER AFRL-IF-RS-TR-1998-174		
9. SPONSORING/MONITORING AGENCY NAME(S) AND ADDRESS(ES) AFRL/IFSB 525 Brooks Road Rome NY 13441-4505		11. SUPPLEMENTARY NOTES AFRL Project Engineer: Donald R. Pflug/IFSB/(315) 330-4290		
12a. DISTRIBUTION AVAILABILITY STATEMENT Approved for public release; distribution unlimited.		12b. DISTRIBUTION CODE		
13. ABSTRACT (Maximum 200 words) The progressive elevation of clock speeds in digital electronic circuits is compelling the merging of design considerations for such circuits with those of analog microwave circuits. For sufficiently high clock rates digital circuits develop substantial analog effects, such as coupling and radiation, that markedly affect the flow of signal pulses in such structures as multilayer circuit boards and multichip modules resulting in unreliable circuit or device operation. Traditional circuit models such as SPICE cannot account for the distributed field physics inherent in these processes. To accurately analyze and design complex digital circuits above 500 MHz, it is necessary to resort to full-wave Maxwell's equations simulations to rigorously compute the electromagnetic field environment within the circuit. The goal of this effort was to initiate the development of electromagnetic models which serve as a bridge between electromagnetic field analysis, nonlinear circuit analysis and CAD/CAM design tools in order to model high speed digital circuits. The computational methodology is based on a finite difference-time domain (FDTD) solution of Maxwell's equations which lends itself to analyzing digital circuits and devices accurately in the presence of complex geometry and materials and general digital signals. The bridging models permit the results of FDTD simulation to be formulated in terms of circuit quantities that can be used as input into circuit programs such as SPICE. Such circuit quantities now contain the mutual coupling effects inherent in the full wave Maxwell's equation solution making the circuit solution much more accurate.				
14. SUBJECT TERMS Computational electromagnetics, circuits, multichip modules, finite difference-time domain		15. NUMBER OF PAGES 52		
17. SECURITY CLASSIFICATION OF REPORT UNCLASSIFIED		18. SECURITY CLASSIFICATION OF THIS PAGE UNCLASSIFIED	19. SECURITY CLASSIFICATION OF ABSTRACT UNCLASSIFIED	16. PRICE CODE UL
17. SECURITY CLASSIFICATION OF REPORT UNCLASSIFIED		18. SECURITY CLASSIFICATION OF THIS PAGE UNCLASSIFIED	19. SECURITY CLASSIFICATION OF ABSTRACT UNCLASSIFIED	20. LIMITATION OF ABSTRACT UL

TABLE OF CONTENTS

<u>Report Section</u>	<u>Page</u>
Table of Contents	i
List of Figures	ii
1.0 Objective and Scope	1
2.0 Background	1
3.0 Task 1. Extract Lumped Device Models from FD-TD Electromagnetic Field Data	2
3.1 Transmission Line Parameters and Load Impedance	2
3.2 S-Parameters	4
3.3 Differential Capacitance Calculation	5
3.4 Differential Inductance Calculation	5
3.5 Lumped Inductance Due to a Discontinuity	6
3.5.1 Flux/Current Definition	7
3.5.2 Fitting $Z(\omega)$ or $S(\omega)$ to an Equivalent Circuit	7
3.5.3 Choice of Methods	8
3.6 Digital Signal Processing and Spectrum Estimation Techniques	8
3.6.1 Prony's Method	9
3.6.2 Autoregressive Models	11
3.6.3 System Identification	15
4.0 Task 2: Perform Visualizations Resulting from FD-TD Modeling	17
4.1 Example 1: Coupling Between Parallel Adjacent Via Pins	17
4.2 Example 2: Coupling Between Perpendicular Circuit Traces	19
4.3 Example 3: Arcing Between Circuit Traces Carrying High RF Power	26
5.0 Task 3. Proceed With FD-TD/SPICE Software Development	28
5.1 Introduction	28
5.2 Formulation	28
5.3 Reported Applications	29
5.4 Potential Applications	30
References	30

LIST OF FIGURES

<u>Figure</u>	<u>Page</u>
1. Color visualization of the early-time response of a >20-layer circuit board to a 0.1-ns Gaussian current pulse propagating down a single vertical via pin. The figure depicts the strength of the magnetic field in a vertical cut through the board. There is substantial pin-to-pin crosstalk due to strong coupling of the magnetic field from the excited center via pin to the two adjacent unexcited via pins.	18
2a. Vertical cross-section of 3-D FD-TD model of coupling from a single z-directed signal trace in a commercial very high-speed computer circuit board to three x-directed signal traces. Vertical separation between each metalization plane = 25.4 μm or 1 mil.	20
2b. Plan view of 3-D FD-TD model of coupling from a single z-directed signal trace in a commercial very high-speed computer circuit board to three x-directed signal traces. Lateral (z) separation between each crossing trace = 317.5 μm or 12.5 mils.	21
3a. Time sequence visualizing snapshots of the longitudinal current densities on the signal and crossing traces.	22
3b. Continuation of the time sequence of Fig. 3a.	23
4. Current density distributions at the time of maximum coupling from the signal trace (Line 1) to the first crossing trace (Line 2).	24
5. Potential distributions at the time of maximum coupling from the signal trace (Line 1) to the first crossing trace (Line 2).	25
6. Visualization of the FD-TD-computed amplitude of the sinusoidal steady-state E_x field distribution at the surface of the alumina substrate of the RF power combiner at 837 MHz.	27

Electromagnetic Field Analysis of Digital Circuits and Modules for Electromagnetic Compatibility and Reliability

1.0 OBJECTIVE AND SCOPE

The goal of this project was to initiate the development of bridging software between electromagnetic field analysis, nonlinear circuit analysis, and CAD/CAM tools to model high-speed digital circuits and multichip modules for electromagnetic compatibility and reliability. The computational methodology was based upon the finite-difference time-domain (FD-TD) solution of Maxwell's equations. The result of this research should be the initiation of a novel computational simulation tool that would assist understanding the operation of high-speed electronic devices of high potential value to Rome Laboratory.

This was initially a six-month program, later extended at no additional cost to eight months, that provided partial support for one Ph.D. graduate at Northwestern. Assistance in running FD-TD/SPICE simulations was provided at no cost by Prof. Melinda Piket May and her students at the University of Colorado at Boulder.

2.0 BACKGROUND

The progressive elevation of clock speeds in digital electronic circuits is compelling the merging of design considerations for such circuits with those of analog microwave circuits. This is because digital circuits develop substantial analog effects when their clock rates are high enough. These effects include such full-wave electromagnetic field phenomena as coupling and radiation, and can markedly affect the flow of signal pulses in typical structures such as multilayer circuit boards and multichip modules.

In fact, coupling and radiation can cause unreliable circuit operation. Traditional circuit models such as SPICE do not have the capability to calculate the distributed-field physics inherent in these processes. Especially for digital circuits operating above 500 MHz, it may not be possible to insure reliable operation without resorting to full-wave Maxwell's equations simulations. Such simulation tools must properly account for the physics of UHF and microwave electromagnetic wave energy transport along metal surfaces such as ground planes, or in possibly inhomogeneous dielectric media away from the metal signal paths. Such tools must also be capable of dealing with the complexity of modern engineering designs.

A strong candidate for this role is FD-TD, which is currently in worldwide use in applications relating to radiated and scattered electromagnetic wave interactions with material

structures. This report discusses the application of FD-TD modeling to analyze the electromagnetic wave properties of high-speed electronic circuits in general, making no distinction between digital or analog. We consider the analysis of both passive interconnects and circuit devices, including extraction of lumped-circuit equivalences, S -parameters, and connections to linear and nonlinear loads.

3.0 TASK 1. EXTRACT LUMPED DEVICE MODELS FROM FD-TD ELECTROMAGNETIC FIELD DATA

This section reports means to extract equivalent transmission line, inductance, and capacitance parameters from FD-TD simulations of general 3-D electrical structures. The structures include interconnects, vias, connectors, and power-distribution systems.

The analysis begins with properly connecting the computed electric and magnetic field vector distributions in time and space to the usual circuit quantities of voltage and current:

$$V(t, x_i) = \int_{C_v} \vec{E}(t, x_i) \cdot d\vec{l}, \quad I(t, x_i) = \oint_{C_l} \vec{H}(t, x_i) \cdot d\vec{l} \quad (1)$$

Here, C_v is a contour extending from a defined voltage reference point (usually a ground plane) to the circuit at location, x_i . In many cases, x_i is a point on a metallic strip transmission line (a microstrip) that propagates the dominant TEM mode. In this situation, $V(t, x_i)$ is independent of the choice of C_v if this path is confined to the transverse plane, and C_v can be conveniently chosen to extend in a perpendicular manner from the ground plane to the adjacent surface of the microstrip. Similarly, the selection of the contour C_l to wrap completely around the strip conductor at its surface in the transverse plane provides the local current. Care must be exercised in applying (1) if there is evidence that the circuit path of interest is propagating non-TEM modes; the accuracy of this formulation can degrade rapidly if the TEM assumption is not met.

3.1 Transmission Line Parameters and Load Impedance

Wideband frequency-domain transmission line parameters can be found by applying the Fourier transform to the voltage and current responses of (1) for an impulsive excitation of the line [1]. For example, the line impedance as a function of frequency is obtained from

$$Z_0(\omega, x_i) = \mathcal{F}[V(t, x_i)] / \mathcal{F}[I(t, x_i)] \quad (2)$$

where $\mathcal{F}[]$ is the Fourier transform operator. Further, if $g(t, x_i)$ denotes a voltage or current waveform at $x = x_i$, and $g(t, x_j)$ is the corresponding waveform at $x = x_j$, then the propagation constant γ can be calculated using the following relationship:

$$\mathcal{F}[g(t, x_j)] = \mathcal{F}[g(t, x_i)] e^{-\gamma(\omega)d} \quad (3a)$$

where $d = x_j - x_i$. Rearranging this expression gives γ as a function of frequency:

$$\gamma(\omega) = \frac{1}{d} \ln \left\{ \frac{\mathcal{F}[g(t, x_i)]}{\mathcal{F}[g(t, x_j)]} \right\} \quad (3b)$$

Defining $\gamma(\omega) = \alpha(\omega) + j\beta(\omega)$, the group velocity $v_g(\omega)$ is calculated as

$$v_g(\omega) = \left[\frac{\partial \beta(\omega)}{\partial \omega} \right]^{-1} \quad (4)$$

For an impulsive line excitation, the wideband reflection coefficient from a given transmission line load is calculated using

$$\Gamma(\omega, x_i) = \frac{\mathcal{F}[V_r(t, x_i)]}{\mathcal{F}[V_i(t, x_i)]} \quad (5a)$$

where V_r is the reflected voltage and V_i is the incident voltage observed at x_i . This reflection coefficient is subsequently transformed to the plane of the load via

$$\Gamma_L(\omega) = \Gamma(\omega, x_i) e^{2\gamma(\omega)\ell} \quad (5b)$$

where ℓ is the distance from x_i to the load. The effective load impedance is then

$$Z_L(\omega) = Z_0(\omega, x_i) \left[\frac{1 + \Gamma_L(\omega)}{1 - \Gamma_L(\omega)} \right] \quad (6)$$

where $Z_L(\omega)$, $Z_0(\omega, x_i)$, and $\Gamma_L(\omega)$ are all complex values.

The discussed derivation of impedance does not take into account that the voltage and current values derived from corresponding electric and magnetic fields in the Yee grid are offset from each other by one-half space cell and one-half time step. Ignoring these offsets can lead to errors for certain geometries. Reference [2] reported a simple but effective interpolation that permits the voltage and current data used in the impedance calculation to be at the same space-time point. Given a voltage $V_{i,j,k}$ and adjacent currents $I_{i+1/2,j,k}$ and $I_{i-1/2,j,k}$, the desired spatially interpolated current is

$$I_{i,j,k} = \sqrt{I_{i+1/2,j,k} I_{i-1/2,j,k}} \quad (7)$$

The half time step can be accounted for by multiplying $V_{i,j,k}$ by a factor of $e^{-j\omega\Delta t/2}$. The corrected equation for impedance now becomes

$$Z_0(\omega, x_i) = \mathcal{F}[V(t, x_i)] e^{-j\omega\Delta t/2} / \mathcal{F}[\sqrt{I(t, x_{i+1/2}) I(t, x_{i-1/2})}] \quad (8)$$

Reference [3] reported studies to validate FD-TD modeling of line impedance for the important case of parallel coplanar microstrips. The first studies were done by setting up FD-TD grids for single x -directed microstrips of negligible metalization thickness and a variety of widths over dielectric substrates on the order of 1 mil (0.001 inch) thick. Grid cell size Δ for these cases was on the order of 0.1 mil with Δt on the order of 4.2 fs. In all cases, conductors were "on grid"; that is, they were located at planar loci of tangential E components in the FD-TD lattice that were set to zero for all time steps. Excitation of a microstrip was provided by specifying a Gaussian-pulse time history for a group of collinear electric field components (usually E_z) bridging the gap between the ground plane and the strip conductor at the desired source location. Application of (2) showed the FD-TD-computed values of Z_0 to be virtually independent of frequency up to 1.0 GHz, and on the order of 1% agreement with textbook values [4].

Next, using similar FD-TD grid resolutions, [3] considered single microstrips with finite metalization thickness, possibly fully embedded within a dielectric layer. Here FD-TD predictions were compared to measurements. In one example, a 1.1-mil-thick, 1.4-mil-wide metal strip was assumed to be suspended 1.1 mils above a large ground plane within a 3.1-mil-thick dielectric layer having $\epsilon_r = 3.2$. The FD-TD numerical simulation predicted a flat characteristic impedance of 48Ω up to 1.0 GHz, agreeing with the experimental results to within the measurement uncertainty (about 0.2Ω). The computed variation of Z_0 above 1 GHz was found to be $\pm 2\Omega$. Similar excellent agreement was found for the propagation delay, where the experimental value was 150.5 ± 1.5 ps/inch, while the FD-TD prediction was 149.5 ps/inch.

Reference [3] also reported a study of the impedance and propagation delay of three parallel, coplanar microstrips having finite metalization thickness. Each microstrip had the geometry discussed above and was separated by 3.6 mils from the adjacent lines. Even-mode results were obtained with all three strips excited simultaneously with the same polarity, while odd-mode results were obtained with the two outer strips excited with the opposite polarity relative to the center strip. Results were also observed for the center strip excited with the two outer strips floating. The FD-TD modeling showed that signal propagation on adjacent lines significantly affected the impedance of the line of interest, and to a lesser degree affected its propagation delay. These results were confirmed by laboratory studies which showed an approximate 7Ω elevation of the characteristic impedance for the even-mode excitation, and an approximate 7Ω reduction of the impedance for the odd-mode excitation (both from dc to about 1 GHz).

3.2 S-Parameters

Given a multiport network, wideband complex-valued scattering parameters S_{mn} can be obtained for an impulsive excitation as follows [1,5]:

$$S_{mn}(\omega, x_m, x_n) = \frac{V_m(\omega, x_m)}{V_n(\omega, x_n)} \sqrt{\frac{Z_{0,n}(\omega)}{Z_{0,m}(\omega)}} \quad (9)$$

where $V_m(\omega, x_m)$ is the voltage at port m at observation plane x_m , $V_n(\omega, x_n)$ is the voltage at port n at observation plane x_n , and $Z_{0,m}$ and $Z_{0,n}$ are the characteristic impedances of the lines connected to these ports. For example, to obtain S_{11} , the incident and reflected pulses at port 1 must be known. To obtain S_{21} , we must observe the transmitted pulse emerging at port 2 corresponding to the known incident pulse at port 1.

In most cases, the magnitudes of the S -parameters are the primary data used by engineers to characterize, for example, the filtering properties of a network. The magnitude data are independent of the observation positions on the transmission lines feeding the corresponding ports, assuming that the feeding lines are either infinitely long or matched at their far ends. However, the phases of the S -parameters are clearly a function of the positions of the observation planes. As discussed later, phase data can be important when extracting a lumped-circuit equivalent network from the observed S -parameter variation with frequency [6].

3.3 Differential Capacitance Calculation

The capacitance per unit length of a strip line can be calculated indirectly using (2) and (4) as

$$C(\omega) = \frac{1}{v_g(\omega)Z_0(\omega)} \quad (10)$$

Of more interest is the possibility that this capacitance can also be calculated directly from the electric field that FD-TD simulations provide. Given a designated incremental $\Delta x \Delta y$ surface patch ΔA on the bottom of a circuit trace (facing the ground plane), Gauss's Law can be used to calculate the electric charge ΔQ on this patch from the normal component of \vec{E} originating from the patch:

$$\Delta Q = \oint_{S_E} (\vec{D} \cdot d\hat{S}_E) \quad (11a)$$

Here $\vec{D} = \epsilon \vec{E}$ and S_E is a virtual surface positioned parallel to the trace and between ΔA and the ground plane that captures all of the electric flux emanating from ΔA . Combined with the voltage expression of (1), the incremental trace capacitance (in farads/meter) is given by the ratio of the charge on ΔA to the voltage

$$\frac{\Delta C}{\Delta x} = \frac{\Delta Q}{V} \quad (11b)$$

This approaches the true differential capacitance per unit length in the limit that $\Delta x \ll \lambda$ for the smallest relevant wavelength λ present on the trace. In this quasi-static limit, $\Delta C/\Delta x$ is independent of the precise nature of ΔA , S_E , and the excitation of the trace.

Note that for building physically representative models, this procedure lends itself to calculating the capacitance between any two surface regions of any shape. Patch ΔA could be defined to wrap around the entire circuit trace. The conductor at the other end of the integral path used to define the voltage (i.e., the other node of the capacitor), could be an adjacent trace rather than the ground plane. This electric flux collection method can directly provide the equivalent mutual capacitance for subsequent SPICE calculations of crosstalk.

3.4 Differential Inductance Calculation

In a manner analogous to that discussed above, the differential inductance of a circuit trace geometry can be calculated directly from the magnetic field vector components that FD-TD simulations provide. It is well known that the self and/or mutual inductance of any physical

structure is entirely determined by the geometric relationship between the electric circuit that transports the current I and the surface S_m through which the magnetic flux generated by I penetrates. In fact, inductance is defined to be the ratio of the magnetic flux penetrating S_m to its generating current

$$L = \frac{\phi}{I} = \frac{\iint_{S_m} \vec{B} \cdot d\hat{S}_m}{I} \quad (12)$$

To obtain inductance from the full-wave electromagnetic field, it is crucial to properly define the magnetic flux collection virtual surface, S_m . Consider the case of no discontinuities of Circuit Trace No. 1, which carries the signal current, I_1 , and the underlying ground plane, which carries the return current, i_1 . Here, we define a planar rectangular "window pane" surface, $S_{m,1}$, that has a perimeter bounded on the top by Trace No. 1, bounded on the bottom by the ground plane, and extends a short distance Δx along the trace. The incremental self-inductance of Trace No. 1 (in henrys/meter) is given by

$$\frac{\Delta L_{11}}{\Delta x} = \frac{\Delta \phi_{11}}{I_1} = \frac{\iint_{S_{m,1}} \vec{B}_1 \cdot d\hat{S}_{m,1}}{I_1} \quad (13)$$

where \vec{B}_1 is the magnetic field generated by I_1 . The incremental mutual inductance relative to a possible adjacent trace (Trace No. 2) is found by obtaining the magnetic flux penetrating $S_{m,1}$ due to current I_2 flowing on Trace 2:

$$\frac{\Delta L_{21}}{\Delta x} = \frac{\Delta \phi_{21}}{I_2} = \frac{\iint_{S_{m,1}} \vec{B}_2 \cdot d\hat{S}_{m,1}}{I_2} \quad (14)$$

where \vec{B}_2 is the magnetic flux generated by I_2 . The inductance values of (13) and (14) approach the true differential inductance per unit length in the limit that $\Delta x \ll \lambda$ for the smallest relevant wavelength λ present on the trace. In this quasi-static limit, $\Delta L/\Delta x$ is independent of the precise nature of S_m and the excitation of the trace.

3.5 Lumped Inductance Due to a Discontinuity

A key element of current engineering practice in the design of high-speed circuits is the development of lumped-circuit equivalences (especially inductances) for discontinuities in the signal and ground return paths. The equivalent circuits for the discontinuities are then substituted into SPICE or SPICE-like circuit modeling software to obtain the desired overall circuit response. Using the Fourier-transformed FD-TD fields, the desired equivalent circuits may be derived in two ways [6]: (1) the basic flux/current definition of inductance, and (2) the fitting of an equivalent circuit to the calculated variation of impedance or S -parameters with frequency. These approaches are now summarized.

3.5.1 Flux/Current Definition

The simple magnetic flux collection procedure discussed in Section 3.4 may be extended to any three-dimensional circuit trace geometry, including the interesting cases of a via present in the signal path and a geometrical discontinuity present in the current return path. Consider for example a microstrip that traverses an open hole or slot discontinuity in the ground plane. Here the use of the planar "window-pane" integration surface $S_{m,1}$ between the slot and the circuit trace would underreport the inductance of the discontinuity, because a portion of the magnetic flux in the open hole or slot would slip under its collection area. But we note that the magnetic flux is always contained between the signal and the return current paths. Thus, it is essential that the *edges* of S_m are bounded by the signal and return currents to collect all of the magnetic flux. Then the total magnetic flux penetrating S_m would be independent of the precise surface definition of S_m .

We see that the problem reduces to finding the return current path and then constructing an integration surface bounded by this path and by the signal trace. One possibility for S_m is a box-like or "hockey net" integration surface. Similar to the "window pane," this S_m has a perimeter bounded on the top by the circuit trace of interest. However, this S_m is bounded on the bottom by the ground plane along a path that is *curved around the hole or slot* to follow the distorted return current path. In this manner, S_m captures substantially all of the local magnetic flux and properly yields the inductance of the discontinuity. For simplicity, we assign four flat rectangular walls to define the S_m "hockey net," noting again that the flux calculation is dependent upon the location of the edges of the net rather than its surfaces. Of course, this Cartesian integration surface is natural for the Yee grid.

3.5.2 Fitting $Z(\omega)$ or $S(\omega)$ to an Equivalent Circuit

A second approach for obtaining the equivalent lumped inductance due to a discontinuity such as a via or a slotted ground plane is to fit the calculated impedance or S -parameter variation with frequency to that of an equivalent circuit over a frequency range of interest [7-9]. For relatively complex geometries consisting of several package planes, vias, and microstrips embedded in multilayered inhomogeneous media, the fitting process can be automated to an extent by using a software package such as EEsof's TOUCHSTONE[®] to manipulate the components in an equivalent circuit composed of a number of inductor-capacitor-resistor (LCR) sections [9]. The inductors model the vias, microstrip traces, and ground return discontinuities, while the capacitors account for the coupling between the package planes. Resistors are associated with internal impedances of sources, lossy materials, and leakage radiation from the circuit planes. The distributed nature of these processes is modeled by using several LCR sections.

For situations where an equivalent circuit is needed over only a limited range of frequencies, Reference [9] reported an alternative to the use of a sophisticated software. This approach is suitable for deriving a simple equivalent circuit by means of a rational function representation of the input impedance:

$$Z_{in}(s) = \frac{V(s)}{I(s)} = R_{in}(s) + jX_{in}(s) \approx \frac{\sum_{i=0}^M a_i s^i}{\sum_{k=0}^N b_k s^k} \quad (15)$$

where $s = j2\pi f$ (for f spanning the desired range of frequencies), and the summation orders M and N are selected by the user to achieve a balance between the accuracy of the impedance-fitting process and the complexity of the resulting equivalent circuit. The unknown real coefficients a_i and b_k can be determined by using either a least-squares minimization procedure or an interpolation method to achieve a best-fit to the variation of impedance with frequency obtained from the FD-TD modeling. Subsequently, these coefficients are used to synthesize an equivalent circuit that is valid in the desired range of frequencies.

3.5.3 Choice of Methods

Reference [6] provided data indicating that certain important distributed components, such as ground pads connected to the ground plane using vias, cannot be easily modeled using the fitting procedure of Section 3.6.2. The key data provided (see Fig. 8 of [6]) indicate that the phase of S_{11} (equivalently, the phase of Z_{in}) can have a dramatically different variation with frequency depending upon the choice of the reference plane. This sensitivity to the observation point makes it very hard to find an equivalent inductance that is independent of the location of the observation plane and also independent of frequency.

On the other hand, [6] reported that the inductance calculated using the flux/current method was found to be essentially independent of frequency (see Fig. 9 of [6]) and "very accurate." For such components, [6] stated that:

As a result, the use of the scattering parameters for the derivation of a simple equivalent circuit becomes much less successful as it compares to the previously mentioned approach which is based on the flux/current definition.

Therefore, the fitting procedure of Section 3.6.2 may not be as robust as the more basic flux/current definition of inductance of Section 3.6.1.

3.6 Digital Signal Processing and Spectrum Estimation Techniques

Typical FD-TD models of high-speed circuit structures use a grid resolution Δ that is dictated by the very fine dimensions of the circuit board layers, vias, and similar components. This resolution is almost always *much finer* than needed to resolve the smallest spectral wavelength propagating in the circuit. As a result, with the time step Δt bound to Δ by numerical stability considerations, it is very common to run FD-TD simulations for tens of thousands of time steps in order to fully evolve the impulse responses needed for calculating impedances, S -parameters, and resonant frequencies of passive structures in electronic circuits operating at UHF and microwave frequencies.

A brute-force way to mitigate the burden of lengthy FD-TD simulations is to simply truncate a run before the impulse response has fully evolved. However, this truncation has the effect of viewing the true time-domain response through a rectangular window of duration $T = N_{\max} \Delta t$.

In the frequency domain, this windowing is translated into the convolution of the true spectrum with the function $\sin(f)/f$. This convolution widens the peaks in the spectral response, causes other distortions, and can mask weak spectral signatures. Distortion can be reduced and the spectral resolution increased only by lengthening the window duration. Unfortunately, this causes FD-TD computer simulation times for several important classes of problems (particularly resonators) to be so lengthy as to be virtually prohibitive.

Recently, there has been significant progress in addressing this problem. The most fruitful approach has been to apply contemporary analysis techniques from the discipline of digital signal processing and spectrum estimation. The strategy is to extrapolate the electromagnetic field time waveform by 10:1 or more beyond the actual FD-TD time-stepping window, allowing a very good estimate of the complete system response with 90% or greater reduction in the FD-TD computation time. In effect, a low-computational-burden extrapolation process at a *limited number* of reflection or transmission observation points in the grid replaces the computationally intensive FD-TD process that is necessarily applied at *every point* in the grid. Then the reflected and transmitted field spectra and the associated impedances and *S*-parameters at the observation points can be efficiently obtained by FFT of the extrapolated waveforms or, in certain cases, from the coefficients of the extrapolation process itself.

This section discusses a number of digital signal processing and spectrum estimation techniques that have appeared in the recent FD-TD literature. While good results have been obtained with each of these methods for appropriate classes of modeling problems, there are emerging tradeoff considerations as FD-TD practitioners become more familiar with the state of the art of modern signal-processing theory. A goal of this section is to illuminate the tradeoffs as currently understood.

3.6.1 Prony's Method

Prony's method [10] has been used to extrapolate transmission-line matrix (TLM) and FD-TD-computed waveforms for microwave circuits by a number of investigators [11-13]. Because it is a technique for modeling sampled data as a linear combination of complex exponentials, it is particularly suitable for calculating the resonant frequency and *Q* of a resonating structure, since the impulse response of such a structure is characterized by a superposition of decaying exponentials. While Prony's method is not a spectral estimation technique in the usual sense, it is closely related to the least-squares linear prediction methods used for parametric spectral estimation [12].

To begin our discussion, let us assume the existence of *N* equally spaced time samples of the FD-TD-computed impulse response of a reflected or transmitted field component *f* at observation point (*i, j, k*) in a high-speed circuit:

$$\left\{ f|_{i,j,k}^{M \rightarrow M+N-1} \right\} \equiv f|_{i,j,k}^M, f|_{i,j,k}^{M+1}, f|_{i,j,k}^{M+2}, \dots, f|_{i,j,k}^{M+N-1} \quad (16)$$

These samples constitute an observation "window" that begins at time step *M* and ends at time step *M + N - 1*. (Note that $\{f\}$ is obtained by *decimating* the actual FD-TD data record at point (*i, j, k*) by a factor of 10 or greater. The FD-TD data are very oversampled relative to

what is needed for Prony's method and the other digital signal processing methods discussed in this section.) Now let each time sample in $\{f\}$ be approximated by a sum of p exponentials:

$$f_{i,j,k}^n = \sum_{\ell=1}^p C_{\ell} e^{(\alpha_{\ell} + j2\pi f_{\ell})(n-M)\Delta t} \equiv \sum_{\ell=1}^p C_{\ell} e^{A_{\ell}(n-M)} \equiv \sum_{\ell=1}^p C_{\ell} (\mu_{\ell})^{n-M} \quad (17)$$

where $0 \leq n - M \leq N - 1$, C_{ℓ} is the complex-valued amplitude of the ℓ th mode, $A_{\ell} = (\alpha_{\ell} + j2\pi f_{\ell})\Delta t$ specifies the modal damping factor and frequency of the ℓ th mode, and p is the order of the model.

The direct solution of (17) is a difficult nonlinear least-squares problem. An alternative solution is based on Prony's method. This is a two-step procedure [10] which solves two sequential sets of linear equations with an intermediate polynomial rooting step that concentrates the nonlinearity of the problem. Following [14], the first step is to set up $N - p$ equations for the p values of A_{ℓ} :

$$\begin{aligned} f_{i,j,k}^{M+p} + A_1 f_{i,j,k}^{M+p-1} + A_2 f_{i,j,k}^{M+p-2} + \dots + A_p f_{i,j,k}^M &= 0 \\ f_{i,j,k}^{M+p+1} + A_1 f_{i,j,k}^{M+p} + A_2 f_{i,j,k}^{M+p-1} + \dots + A_p f_{i,j,k}^{M+1} &= 0 \\ \vdots & \\ f_{i,j,k}^{M+N-1} + A_1 f_{i,j,k}^{M+N-2} + A_2 f_{i,j,k}^{M+N-3} + \dots + A_p f_{i,j,k}^{M+N-1-p} &= 0 \end{aligned} \quad (18)$$

This overdetermined system is solved using a least-squares algorithm for the $\{A_{\ell}\}$. This permits the $\{\mu_{\ell}\}$ to be found as the roots of the polynomial

$$\mu^p + A_1 \mu^{p-1} + A_2 \mu^{p-2} + \dots + A_{p-1} \mu + A_p = 0 \quad (19)$$

The second step is to find the $\{C_{\ell}\}$ in (17). This is accomplished by writing out (17) for each of the time samples, thereby obtaining a set of N equations in the p values of the C_{ℓ} :

$$\begin{aligned} C_1 + C_2 + \dots + C_p &= f_{i,j,k}^M \\ \mu_1 C_1 + \mu_2 C_2 + \dots + \mu_p C_p &= f_{i,j,k}^{M+1} \\ (\mu_1)^2 C_1 + (\mu_2)^2 C_2 + \dots + (\mu_p)^2 C_p &= f_{i,j,k}^{M+2} \\ \vdots & \\ (\mu_1)^{N-1} C_1 + (\mu_2)^{N-1} C_2 + \dots + (\mu_p)^{N-1} C_p &= f_{i,j,k}^{M+N-1} \end{aligned} \quad (20)$$

This overdetermined system is solved using a least-squares algorithm for the $\{C_i\}$. Now all of the parameters in (17) are known, and it becomes very easy to:

1. Write down by inspection the set of resonant frequencies and Q-factors ($Q_i = |\pi f_i / \alpha_i|$) directly from the Prony parameter sets just obtained;
2. Calculate the complete estimated impulse response at times $n \gg M + N - 1$ until it is observed to decay to zero, at which point an FFT provides the magnitude and phase of the frequency-domain transfer function with no windowing artifacts.

Reference [13] reported results using Prony's method for the resonant frequencies and Q's of the three lowest TE_{0n} modes of a cylindrical dielectric resonator of permittivity $\epsilon_r = 38$, radius $a = 5.25$ mm, and length $l = 4.6$ mm. A cylindrical FD-TD grid was used, with parameters $\Delta r = 0.29167$ mm, $\Delta z = 0.2875$ mm, and $\Delta t = 0.4795$ ps. A time-stepping window extending over about 2^{17} (131,072) steps was needed to obtain converged results for the Q of the TE_{02} mode when using an FFT applied to the windowed FD-TD data. However, using Prony's method of order $p = 10$ and a decimation factor of 50, only 3000 time steps were required to obtain the same Q, a reduction of about 98%. In fact, reductions can be *even greater* in the case of structures having even higher Q or with very closely spaced resonant frequencies.

Prony's method shows good resolution with relatively short data sequences and presents no windowing problem. The main difficulty with this approach lies in its determination of p , the user-selected order of the model. If the value of p is less than the number of actual modes excited in the structure, the spectral resolution is poor. However, if p is selected to be too high, spurious (nonphysical) modes appear. The following are two guidelines given in [13] to deal with these problems:

- Before Prony's method is applied, digitally low-pass filter the time-domain response to limit the number of resonant modes and therefore the number of parameters to calculate.
- If spurious modes are suspected, apply Prony's method with the time sequence of the sample points in reverse order. Here the real modes appear with positive damping factors ($\alpha_i > 0$), but the spurious modes have negative damping factors ($\alpha_i < 0$) [15].

3.6.2 Autoregressive Models

The most popular time series modeling approach used in modern spectral estimation is the class of linear predictors or autoregressive (AR) models. This is because an accurate estimate of the AR parameters can be derived by solving a set of linear equations. In contrast to Prony's method, which uses a sum of deterministic exponential functions to fit the data, the AR approach constructs a random model to fit a statistical data base to the second-order.

We again assume the FD-TD-computed impulse response of (16), i.e., N equally spaced time samples beginning at time step M . This time series is said to represent the realization of an AR process of order p if it satisfies the following relation:

$$f_{i,j,k}^n = -a_1 f_{i,j,k}^{n-1} - a_2 f_{i,j,k}^{n-2} - \dots - a_p f_{i,j,k}^{n-p} + q(n) \quad (21)$$

where the constants a_1, a_2, \dots, a_p are the AR parameters to be determined from $\{f\}$, and $q(n)$ is a white noise process whose variance also has to be found to carry out the extrapolation of $\{f\}$. It is clear that (21) permits the prediction of a new value of the time series from known previous values once the AR parameters are in hand.

There exists many published approaches to evaluating the a_i [16]. In fact, a primary categorization of AR techniques is by the means used to calculate these parameters. In this section, we consider three specific recent applications of AR to the extrapolation of FD-TD electromagnetic field records, categorized according to this criterion: (1) the covariance method, (2) the forward-backward method, and (3) the nonlinear predictor. The choice of approach is very important, since these three methods have substantially different operational characteristics.

Covariance Method

Reference [17] reported the use of the covariance method for determining the AR parameters. This method involves setting up and solving the following $p \times p$ linear system of equations:

$$\begin{bmatrix} c_{ff}(1,1) & c_{ff}(1,2) & \dots & c_{ff}(1,p) \\ c_{ff}(2,1) & c_{ff}(2,2) & \dots & c_{ff}(2,p) \\ \vdots & \vdots & \ddots & \vdots \\ c_{ff}(p,1) & c_{ff}(p,2) & \dots & c_{ff}(p,p) \end{bmatrix} \begin{bmatrix} a_1 \\ a_2 \\ \vdots \\ a_p \end{bmatrix} = - \begin{bmatrix} c_{ff}(1,0) \\ c_{ff}(2,0) \\ \vdots \\ c_{ff}(p,0) \end{bmatrix} \quad (22)$$

where c_{ff} are covariances defined by

$$c_{ff}(\alpha, \beta) = \frac{1}{N-p} \sum_{n=p}^{N-1} (f|_{i,j,k}^{M+n-\alpha} f|_{i,j,k}^{M+n-\beta}) \quad (23)$$

The matrix of (22) is Hermitian and positive semidefinite, and can be solved by Cholesky decomposition.

As stated in [17], a key issue that arises when using the covariance-based AR model is choosing the order of the model, p . The use of a low-order AR model of this type causes the extrapolated waveform to attenuate quickly in a nonphysical manner. To compensate, a high-order model is required. However, a high-order model can cause divergence problems in some cases because of statistical instabilities introduced by the large order. These competing effects cause the results of the covariance-based AR model to be sensitive to the model order, diminishing its usefulness somewhat. Two commonly used ways to estimate p are the final prediction error technique and the Akaike Information Criterion [18]. Both are based upon the estimated predictor error power and are regarded as general guides for AR model selection.

Using the covariance-based AR method of (22) and (23), [17] reported the successful extrapolation to over 30,000 time steps of FD-TD field records spanning only 2000 to 3500 time steps. A decimation factor of 10 was used, and the order of the AR model was 50. Another example discussed in [17] involved modeling a strip line double-stub structure that required a substantial computation space because of the large ratio of the maximum to minimum dimensions of the structure. Here, the lengthy wave propagation delays along the stubs required

extrapolating the FD-TD data to 100,000 time steps to achieve convergence of the transmission coefficient. This extrapolation was accomplished using a 91st-order AR model working from an FD-TD data base covering iterations 3100 to 8900, and decimated by a factor of 25. Although very good agreement was observed with benchmark frequency-domain data, the results of the AR model were found to be very sensitive to the order of the model, much more so than the 50th-order model used for the previous two examples.

Forward-Backward Method

The results of a covariance-based AR model can be sensitive to the order of the model, because its a_i parameters often have low accuracy. The low accuracy results, in turn, because the ensemble calculation that is rigorously required to find the covariance is instead substituted in these methods by using the law of large numbers and by approximating the covariance with inexact functions of the known time signal. A useful alternative approach based on an unconstrained least-squares estimation of the AR parameters was proposed independently in [19] and [20] and calculated more efficiently in [21]. This approach, called the *forward and backward prediction method* [20], was used for the first time in [22] to extrapolate FD-TD-computed field records. It avoids the problems of the covariance-based AR models by working directly with the time-domain data, rather than calculating the covariance functions of the data.

Reference [21] reported setting up the following $(p + 1) \times (p + 1)$ linear system of equations for the forward-backward method:

$$\begin{bmatrix} r(0, 0) & \dots & r(0, p) \\ \vdots & \ddots & \vdots \\ r(p, 0) & \dots & r(p, p) \end{bmatrix} \begin{bmatrix} 1 \\ a_1 \\ a_2 \\ \vdots \\ a_p \end{bmatrix} = \begin{bmatrix} e_p \\ 0 \\ 0 \\ 0 \\ 0 \end{bmatrix} \quad (24)$$

where, for $0 \leq \alpha, \beta \leq p$, we have

$$r(\alpha, \beta) = \sum_{\ell=1}^{N-p} \left(f_{i,j,k}^{M+p+\ell-\beta} f_{i,j,k}^{M+p+\ell-\alpha} + f_{i,j,k}^{M+\ell+\beta} f_{i,j,k}^{M+\ell+\alpha} \right) \quad (25a)$$

$$e_p = \sum_{\ell=0}^p a_\ell r(0, \ell) \quad (25b)$$

Reference [21] proved that matrix $[r(\alpha, \beta)]$ of (24) is always positive semidefinite; and if it is nonsingular, then it is positive definite. This is the most common case, since otherwise the recursive determination for the AR parameters would not be possible. Reference [21] also derived an elegant algorithm to solve the linear system of (24) without inverting $[r(\alpha, \beta)]$, thereby requiring only $O(p^2)$ arithmetic operations. However, this sophistication does not appear to be necessary when extrapolating just a few FD-TD records having a size (after

decimation) of perhaps a few hundred data points, and an AR model order p of 50 or less. In fact, [19, 20] successfully solved (24) for the $\{a\}$ using simple matrix inversion.

Reference [21] reported favorable results for the forward-backward method versus existing popular AR approaches such as the Burg algorithm and the Yule-Walker algorithm. The generated AR spectra had less bias in the frequency estimate of the spectral components, reduced variance in frequency estimates over an ensemble of spectra, and no spectral line splitting. Much of the performance improvement was attributed in [21] by the removal in the forward-backward method of the constraint that the estimation procedure always place poles inside the unit circle in the z -transform plane. It is clear that the removal of this constraint presents a potential instability, indicating the need for caution when using this method. However, based upon the results of over 3000 spectra with varying signal-to-noise ratios generated from actual data records via the forward-backward method, [21] noted that fewer than 1% had poles outside of the unit circle. In addition, [20] found no unstable poles when simulating narrowband processes. Overall, these findings indicate that the forward-backward method is sufficiently robust for practical engineering application and is an attractive alternative to the Burg and related algorithms for AR spectral estimation.

Reference [22] was the first to report the application of the forward-backward method to AR extrapolation of FD-TD data records and corresponding spectral estimation. Results were given for a test problem involving a rectangular PEC plate embedded in a high-permittivity half space and excited by a sinusoidal point source located in the free-space region. Both an autocorrelation-based Yule-Walker AR model and the forward-backward AR model were "trained" on the same FD-TD field waveform record, data points from 201 to 800 time steps ("appropriately decimated and low-pass filtered"). Both models were then used to generate an extrapolated sequence extending over 5000 time steps. The forward-backward method exhibited two key advantages relative to the Yule-Walker method: (1) It provided more accurate spectra, and (2) Its order was much lower, $p = 5$ versus $p = 50$. It was concluded in [22] that the forward-backward AR model appears to provide a very good approach to FD-TD signal extrapolation and spectrum estimation both in terms of accuracy and speed.

Nonlinear Predictor

In addition to the use of covariance-based AR linear prediction to extrapolate FD-TD waveform records (discussed earlier), [17] reported the application of a nonlinear predictor for the same purpose. The basic form of this predictor was the exponential autoregressive (EXPAR) model of order p given by [23,24]:

$$f_{i,j,k}^n = \sum_{t=1}^p \left\{ a_t + b_t \exp \left[-\delta \left(f_{i,j,k}^{n-t} \right)^2 \right] \right\} f_{i,j,k}^{n-t} + \text{error term} \quad (26)$$

where $\{a\}$, $\{b\}$, and δ are the modeling parameters that are "trained" from the windowed and decimated FD-TD field-versus-time record.

The EXPAR model was applied in [17] to the same large double-stub strip line problem discussed earlier in [17], and similarly used to extrapolate an 8900-step FD-TD data record to 100,000 time steps. The nonlinear EXPAR model provided excellent accuracy for S_{21} over a

wide dynamic range upon Fourier transformation of the 100,000-step record. Moreover, the EXPAR results were much less sensitive to the model order than were the results of the 91st-order covariance-based linear AR model. However, the reported order of the EXPAR model in this paper exceeded 80, still very high. A necessary line of inquiry involves applying the forward-backward linear AR model to problems of this size and complexity to establish whether its superior characteristics can markedly reduce the required model order.

3.6.3 System Identification

For a linear system, it is well known that the output signal $y(t)$ is related to the input signal $x(t)$ by the convolution

$$y(t) = h(t) * x(t) \quad (27a)$$

where $h(t)$ is the system impulse response. Rigorously, convolution requires knowledge of the entire time history of $x(t)$. For a discrete-time linear system, the time-domain output/input relation of (27a) can be expressed as the following *nonrecursive weighted sum* of time samples of $x(t)$, assuming zero initial conditions:

$$y|ⁿ = \sum_{\ell=0}^n h(\ell) x|^{n-\ell} \quad (27b)$$

This operation typically characterizes what is called a *finite-duration impulse response* (FIR) filter.

Now consider an alternate *system identification* (SI) approach [25-28] to characterize a discrete-time linear system. This approach specifies the time-domain output/input relation as the following recursive difference equation:

$$y|ⁿ = -\sum_{\ell=1}^N a_{\ell} y|^{n-\ell} + \sum_{\ell=0}^{N'} b_{\ell} x|^{n-\ell} \quad (28)$$

where the system parameter sets $\{a\}$ and $\{b\}$ are initially unknown and must be "trained" on a windowed and decimated portion of the input signal record. Because the SI approach has feedback, it is termed an *infinite-duration impulse response* (IIR) filter. Reference [28] notes that it is known that the IIR filter can provide a less complex, lower-order realization than the FIR filter for low-pass systems. Therefore, the SI IIR formulation of (28) should be more efficient for processing FD-TD data than the convolutional FIR formulation of (27b), since FD-TD is inherently a low-pass system (i.e., its spectrum of space/time Fourier modes is bounded by the Nyquist limit established by the grid sampling).

We now consider the search procedure in $(\{a\}, \{b\})$ space reported by [27] to obtain the optimum system parameter sets. In the context of FD-TD, the process deals with electromagnetic field quantities, so we use the field component f instead of y , and the usual space-time notation. Equation (28) is now written in compact form as the dot product of two one-dimensional arrays:

$$f_{i,j,k}^n = [\Phi_{i,j,k}^{n-1}]^T \cdot [\Theta_0|_{i,j,k}] \quad (29)$$

Here $[\Phi]$ is a data array containing the past and present values of the input and output field samples at grid point (i, j, k) , $[\Theta_0]$ contains the parameter sets $\{a\}$ and $\{b\}$ unique to this grid point, and T denotes the array transpose operation. However, at the beginning of the search procedure (say, time step n), the elements of $[\Theta_0]$ are unknown. We make the arbitrary guess $[\hat{\Theta}_0]$. (Reference [27] reported success with the initial guess $[\hat{\Theta}_0] = \bar{0}$, that is, the search beginning at the origin of the $(\{a\}, \{b\})$ space.) Using the existing input and output data records at time step n , an estimate for the output field $\hat{f}_{i,j,k}^n$ can now be obtained in terms of the guessed system parameters:

$$\hat{f}_{i,j,k}^n = [\Phi_{i,j,k}^{n-1}]^T \cdot [\hat{\Theta}_{i,j,k}^{n-1}] \quad (30)$$

The difference between the actual and estimated FD-TD field outputs at time step n is obtained by subtracting (30) from (29), and then minimized with respect to the elements of $\{a\}$ and $\{b\}$. This yields the following system parameter update relations:

$$[\hat{\Theta}_{i,j,k}^n] = [\hat{\Theta}_{i,j,k}^{n-1}] + \frac{[P_{i,j,k}^{n-1}] \cdot [\Phi_{i,j,k}^{n-1}]}{[\Phi_{i,j,k}^{n-1}]^T \cdot [P_{i,j,k}^{n-1}] \cdot [\Phi_{i,j,k}^{n-1}]} \underbrace{\left(f_{i,j,k}^n - \hat{f}_{i,j,k}^n \right)}_{e_{i,j,k}^n} \quad (31)$$

$$[P_{i,j,k}^n] = [P_{i,j,k}^{n-1}] - \frac{[P_{i,j,k}^{n-1}] \cdot [\Phi_{i,j,k}^{n-1}] \cdot [\Phi_{i,j,k}^{n-1}]^T \cdot [P_{i,j,k}^{n-1}]}{[\Phi_{i,j,k}^{n-1}]^T \cdot [P_{i,j,k}^{n-1}] \cdot [\Phi_{i,j,k}^{n-1}]} \quad (32)$$

where $P_{i,j,k}^0 = I$, the identity matrix. The procedure of (31) and (32) is continued until $e_{i,j,k}^n$, the discrepancy between the estimated output and the FD-TD-computed field value, is sufficiently small. At this point, the system parameters at point (i, j, k) have been "trained," and a useful extrapolation of the field record is possible. From a mathematics perspective, this method provides an orthogonal projection search in the system parameter space which usually results in rapid parameter convergence. It is properly called a "least-squares-based system identification projection algorithm for a deterministic autoregressive moving average (ARMA) model."

An ARMA model with system parameters $N = 40$ and $N' = 40$ in (28) was applied in [27] to calculate the resonant frequencies of a PEC rectangular cavity partially filled with a dielectric slab. The cavity was excited at its center plane by imposing a pulsed TE_{10} mode field distribution, and the time waveform of this excitation was used as the input signal $x(t)$ in (28). The parameter search began at $n = 0$ with $\{a\} = \{0\}$, and the parameter values were updated at each FD-TD time step (no decimation). Upon convergence of these parameters, the resonant frequencies of the cavity could be derived with no Fourier transform of the output signal, if desired. Instead, the Z-transform of (28) would be evaluated on the unit circle which is defined

in terms of the system parameters, thereby obtaining the resonant frequencies directly from the poles of the ARMA model.

Overall, the ARMA SI algorithm requires minimal additional computational cost. It provides a rapidly converging recursive processing of the input and output values of the FD-TD simulation, and can be performed concurrently with the usual FD-TD time-stepping at any number of observation points in the grid. In addition to permitting an extrapolation of the local field values at the observation points, the frequency spectrum is immediately available without needing to apply a Fourier transform. Further, the input/output nature of the SI formulation permits an efficient natural treatment of diakoptic splitting of the computation space without needing to use convolutions [28, 29].

4.0 TASK 2. PERFORM VISUALIZATIONS RESULTING FROM FD-TD MODELING

This section reports selected visualizations of propagating signals within commercial circuit boards of contemporary design.¹ Because we are working in the time domain, we can observe the dynamics of potentially important physical phenomena such as reflections, non-uniformities of current flow, edge and corner enhancements, and fields propagating through the dielectric media rather than flowing along the desired metallic signal path.

4.1 Example 1: Coupling Between Parallel Adjacent Via Pins

This example involves the detailed 3-D FD-TD modeling of a very high-speed computer circuit board having more than twenty 0.004-inch thick layers. The board is penetrated by a regular array of 0.012-inch diameter circular via pins located on 0.1-inch centers. A uniform grid cell size of $\Delta = 0.004$ inch is used in the FD-TD model, with a time step $\Delta t = 0.169$ ps. The power and signal metallizations of the circuit board are assumed to be monolayers of tangential electric field components set to zero.

Fig. 1 is a color visualization of the early-time response of the circuit board to a 0.1-ns Gaussian current pulse propagating down a single vertical via pin. The via pin (in a circular via hole) is excited by pulsing a vertical electric field component E_z in the FD-TD grid just above the pin and below a simulated ground strap connected to the ground return. The exciting pulse is selected to have a bandwidth comparable to that of the actual stream of nanosecond digital pulses running through the via (including the harmonic energy in these pulses). Fig. 1 depicts the strength of the magnetic field in a vertical cut through the board, using a color scale of red - yellow - green - blue -violet to visualize maximum to minimum field intensities, respectively. We observe substantial pin-to-pin crosstalk due to strong coupling of the magnetic field from the excited via pin to the adjacent unexcited via pins. In fact, the peak coupled magnetic field (and thus the peak coupled pin current) is down by only about 2 to 3 dB in the via pins immediately adjacent to the excited pin. This represents a potentially very troublesome "self jamming" problem inherent in this circuit board design.

¹The names of the companies involved are not relevant to this discussion and are therefore omitted.

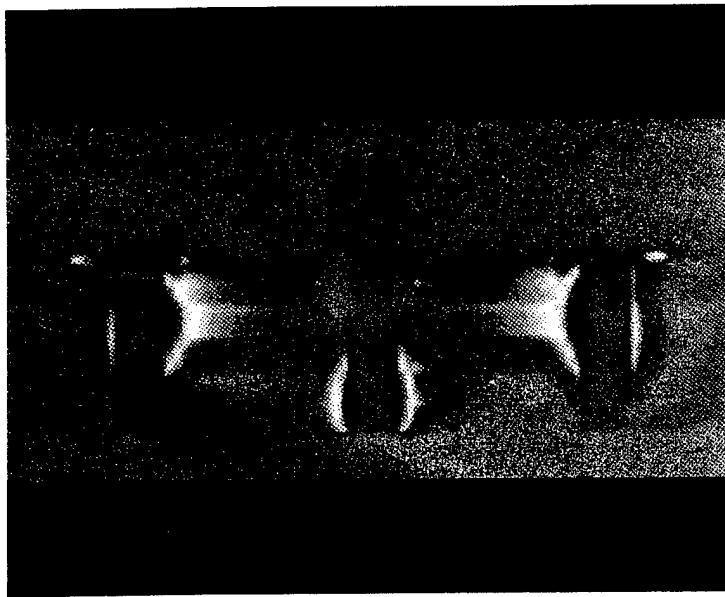


Fig. 1 Color visualization of the early-time response of a >20-layer circuit board to a 0.1-ns Gaussian current pulse propagating down a single vertical via pin. The figure depicts the strength of the magnetic field in a vertical cut through the board, using a color scale of red - yellow - green - blue -violet to visualize maximum to minimum field intensities. There is substantial pin-to-pin crosstalk due to strong coupling of the magnetic field from the excited center via pin to the two adjacent unexcited via pins.

4.2 Example 2: Coupling Between Perpendicular Circuit Traces

This example, constructed especially for this Rome Laboratory program, involves the detailed 3-D FD-TD modeling of coupling from a single signal trace in a commercial very high-speed computer circuit board to three perpendicular signal traces in the adjacent metalization layer. A uniform grid cell size of $\Delta = 12.7 \mu\text{m}$ (equal to 0.0005 inch, or 0.5 mil) is used in the FD-TD model with a time step $\Delta t = 20 \text{ fs}$. As in Example 1, all signal traces of the circuit board are assumed to be monolayers of tangential electric field components set to zero.

Figs. 2a and 2b depict, respectively, the cross-section and plan views of this geometry. The yellow region in each figure denotes the interior of the modeled circuit board filled with a dielectric of $\epsilon_r = 3.0$, and the blue lines denote metallizations. The array of dots represents grid reference points spaced at 5-cell ($63.5 \mu\text{m}$ or 2.5 mils) increments. There is nothing physically located at these dots.

Referring to Fig. 2a, an approximately 30-ps duration Gaussian signal pulse is assumed to be incident into the page (in the $+z$ direction) on the lower trace, which is 3 cells ($38.1 \mu\text{m}$ or 1.5 mils) wide and 2 cells ($25.4 \mu\text{m}$ or 1 mil) above the lower ground plane. There are three crossing traces located in a plane 2 cells ($25.4 \mu\text{m}$ or 1 mil) above the signal trace and oriented perpendicular to it in the x -direction. The upper ground plane is located 2 cells ($25.4 \mu\text{m}$ or 1 mil) above the plane of the three crossing traces.

Referring to Fig. 2b, each of the crossing traces is also 3 cells ($38.1 \mu\text{m}$ or 1.5 mils) wide, with a center-to-center spacing of 25 cells ($317.5 \mu\text{m}$ or 12.5 mils) in the z -direction relative to the adjacent crossing trace. The first of these crosses the signal trace 25 cells ($317.5 \mu\text{m}$ or 12.5 mils) from the source. All traces are terminated in a 4-cell thick Berenger perfectly matched layer (PML) absorbing boundary condition (ABC).

Figs. 3a and 3b visualize a time sequence of snapshots of the longitudinal current density distributions on the signal and crossing traces as indicated by the transverse tangential H -field component at the surface of each trace. (The observation perspective is the plan view of Fig. 2b.) The upper panels show H_x at the plane of the signal trace, thereby providing J_z along the trace. The lower panels show the corresponding H_z at the plane of the crossing traces, thereby providing J_x along these traces. The color scale provides bipolar information, with blue - light blue - white denoting increasingly positive values, and red - yellow - white denoting increasingly negative values. We see that the passage of the $+z$ -directed incident pulse on the signal trace successively induces a rightward ($+x$ -directed) pulse and a leftward ($-x$ -directed) pulse on each of the crossing traces above it which propagate away from the vicinity of the signal trace. The resulting current density values on each crossing trace have odd symmetry in the x -direction about a point just above the signal trace. As the signal pulse leaves the grid, so do the coupled pulses on the crossing lines, due to the action of the PML ABC.

Fig. 4 graphs the spatial distribution of H_x (equivalently, J_z) along the signal trace (Line 1) and H_z (equivalently, J_x) along the first crossing trace (Line 2) at approximately the time of maximum coupling. Fig. 5 graphs the corresponding spatial distributions of the voltage of each line, referenced to the lower ground plane. The peak coupling from the signal trace to the first crossing trace is about -28 dB. This is considerably weaker than the -2 or -3 dB coupling noted in Example 1 (adjacent parallel via pins), and should not present an electromagnetic compatibility problem even at contemporary supercomputer clocks of about 1 GHz.

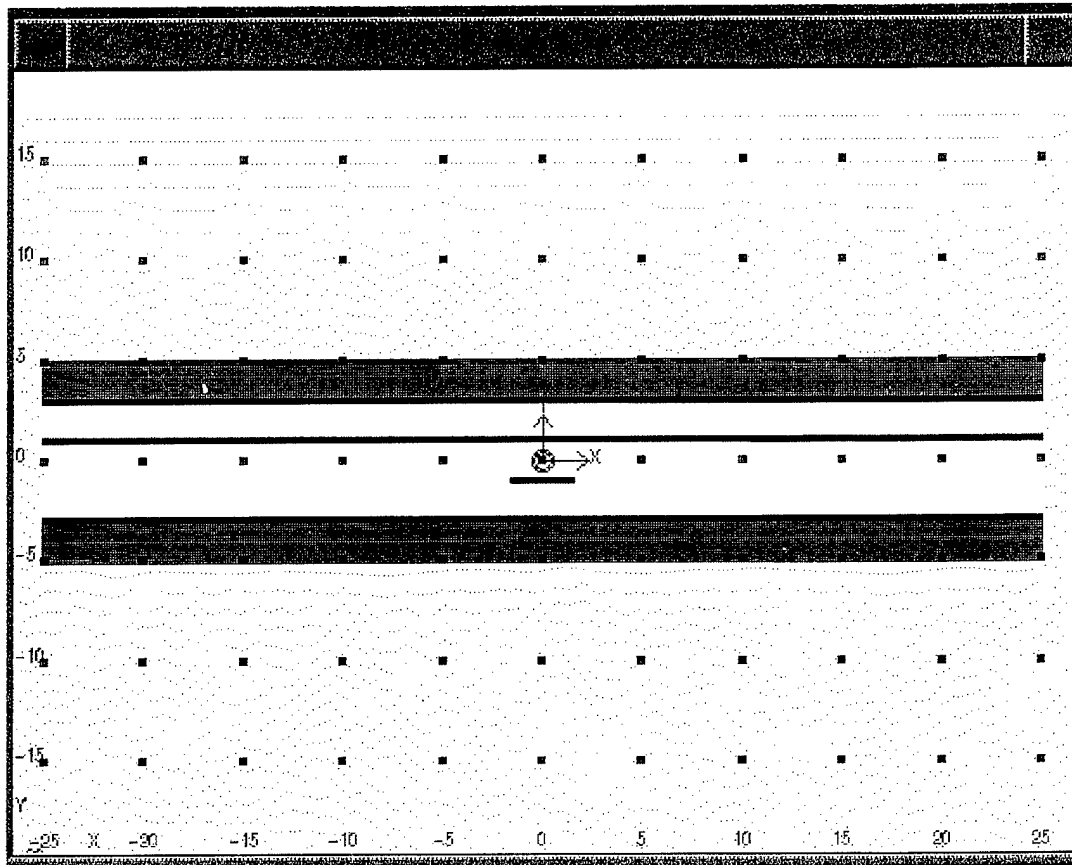


Fig. 2a Vertical cross-section of 3-D FD-TD model of coupling from a single z-directed signal trace in a commercial very high-speed computer circuit board to three x-directed signal traces. Yellow denotes the interior of the circuit board filled with a dielectric of $\epsilon_r = 3.0$; the blue lines denote metallizations. The dots are grid reference points spaced at 5-cell (63.5 μm or 2.5 mils) increments; there is nothing physically located at these dots. Vertical separation between each metalization plane = 2 cells (25.4 μm or 1 mil).

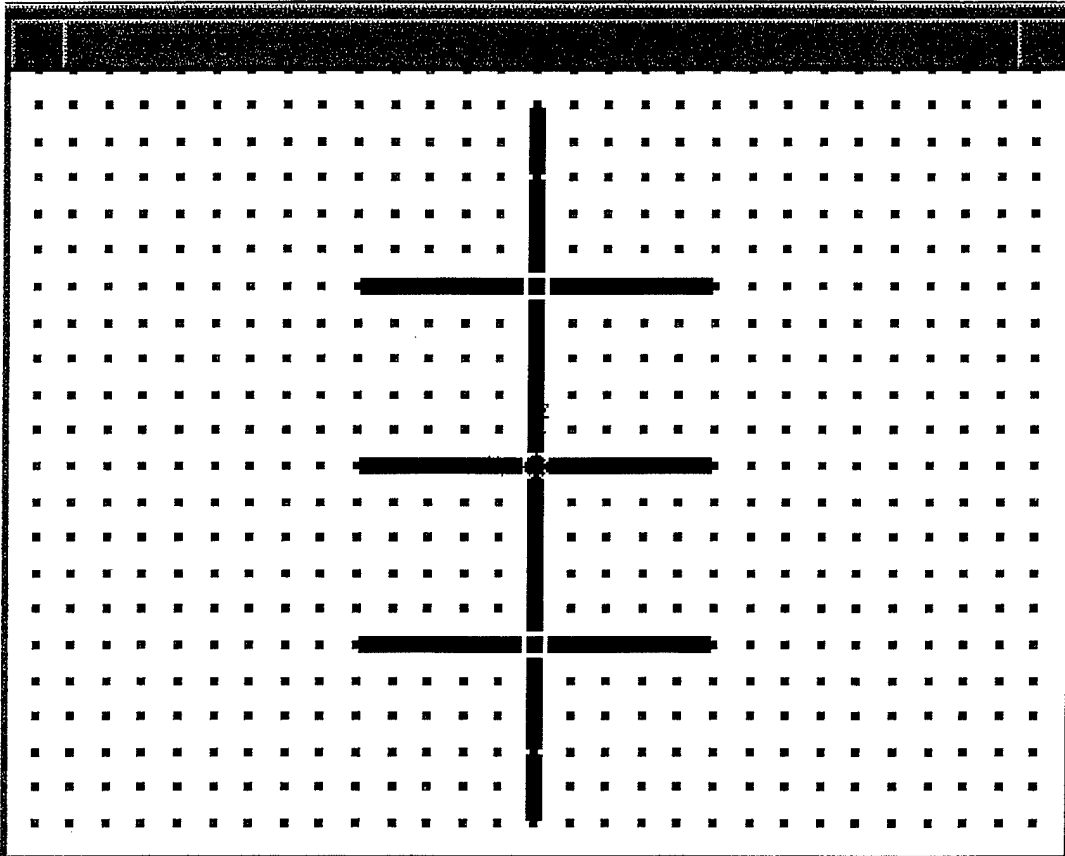


Fig. 2b Plan view of 3-D FD-TD model of coupling from a single z -directed signal trace in a commercial very high-speed computer circuit board to three x -directed signal traces. Yellow denotes the interior of the circuit board filled with a dielectric of $\epsilon_r = 3.0$; the blue lines denote metal traces. The dots are grid reference points spaced at 5-cell ($63.5 \mu\text{m}$ or 2.5 mils) increments; there is nothing physically located at these dots. Lateral (z) separation between each crossing trace = 25 cells ($317.5 \mu\text{m}$ or 12.5 mils).

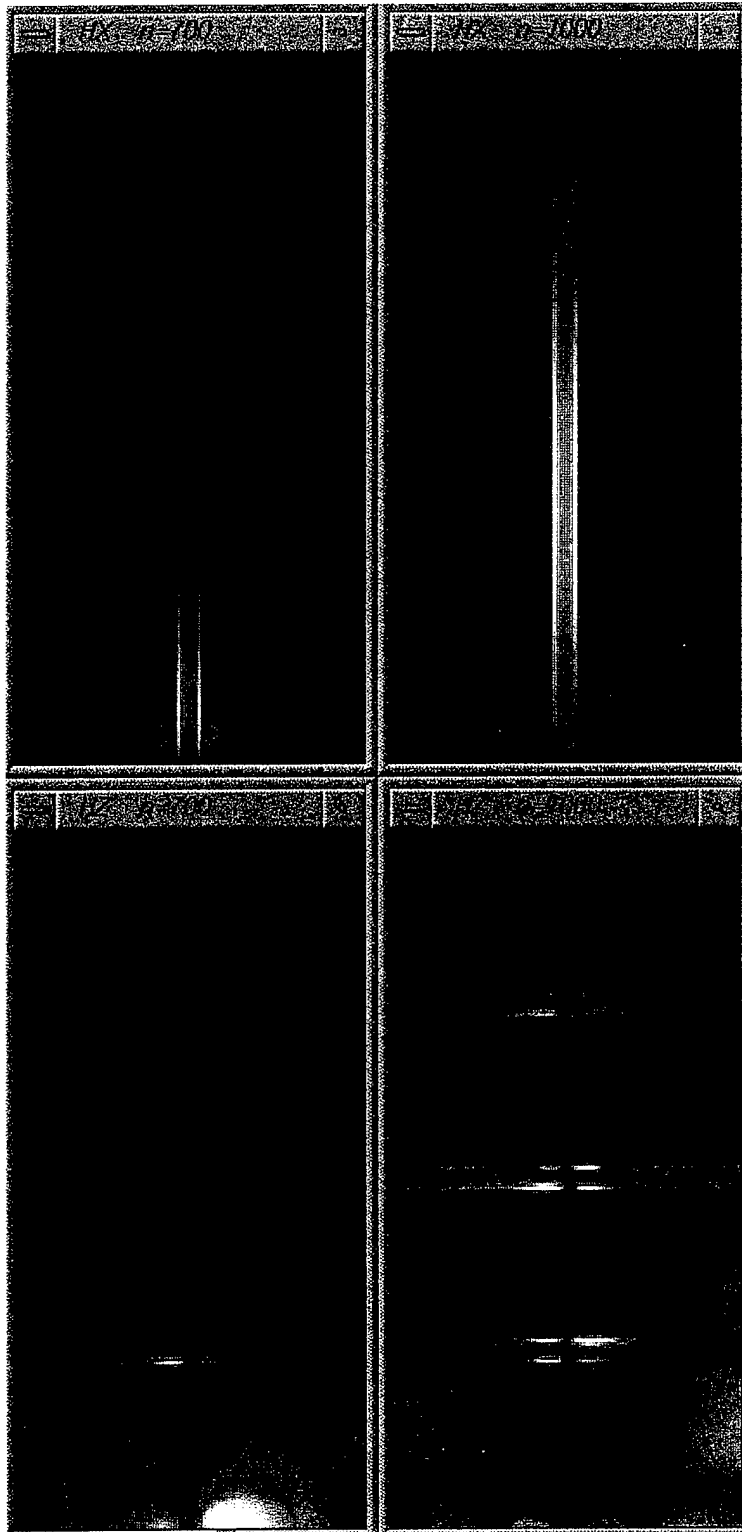


Fig. 3a Time sequence visualizing snapshots of the longitudinal current densities on the signal and crossing traces. Upper panels show H_x at the plane of the signal trace, yielding J_z along the trace. Lower panels show the corresponding H_z at the plane of the crossing traces, yielding J_x along these traces. Color scale: blue - light blue - white show increasingly positive values; red - yellow - white show increasingly negative values.

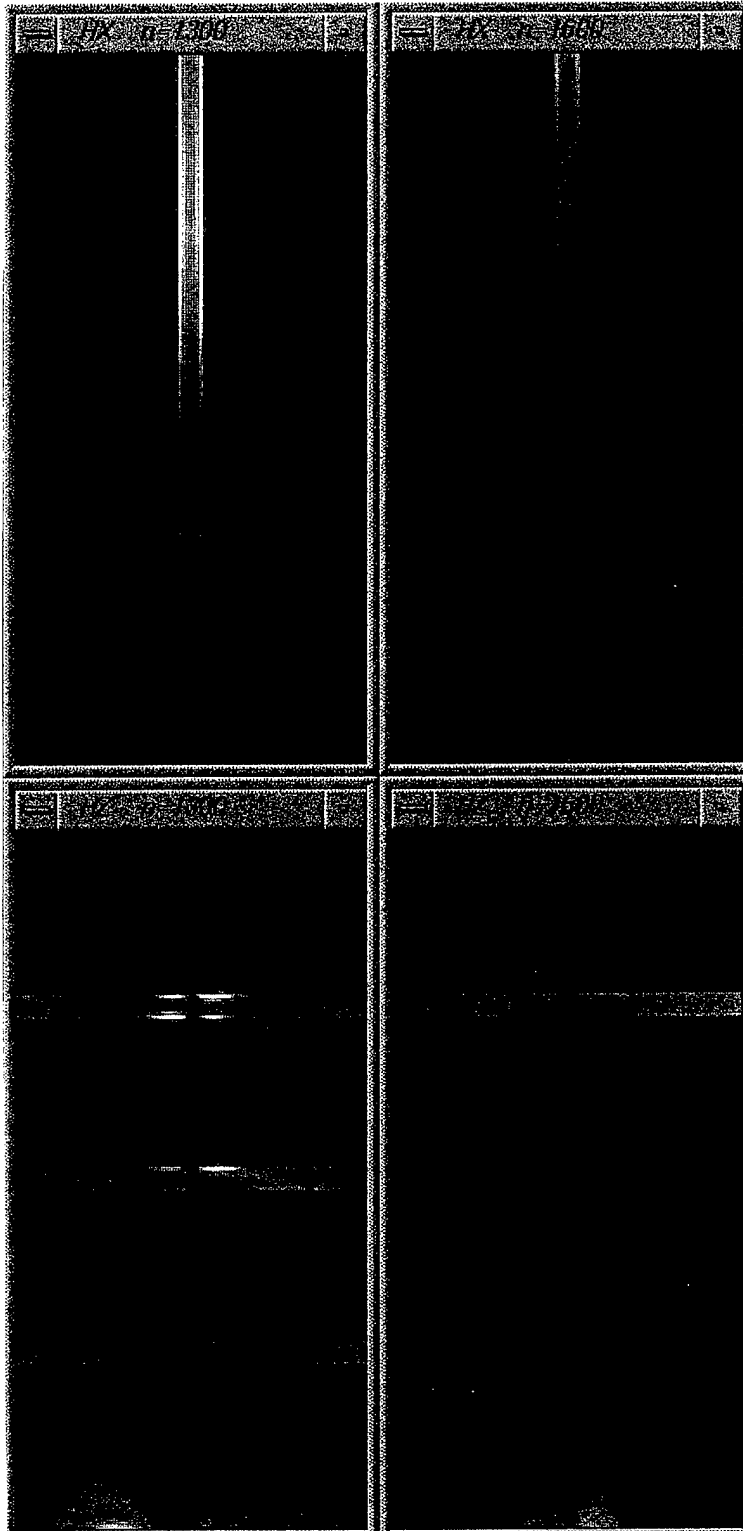


Fig. 3b Continuation of the time sequence of Fig. 3a.

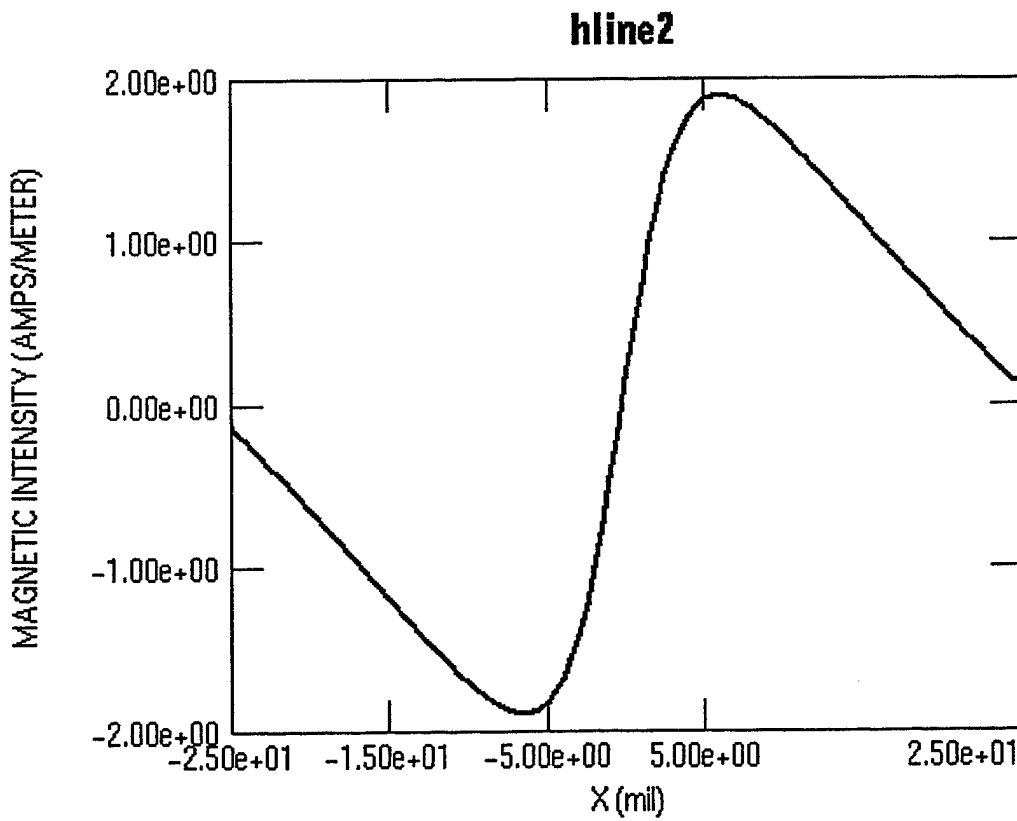
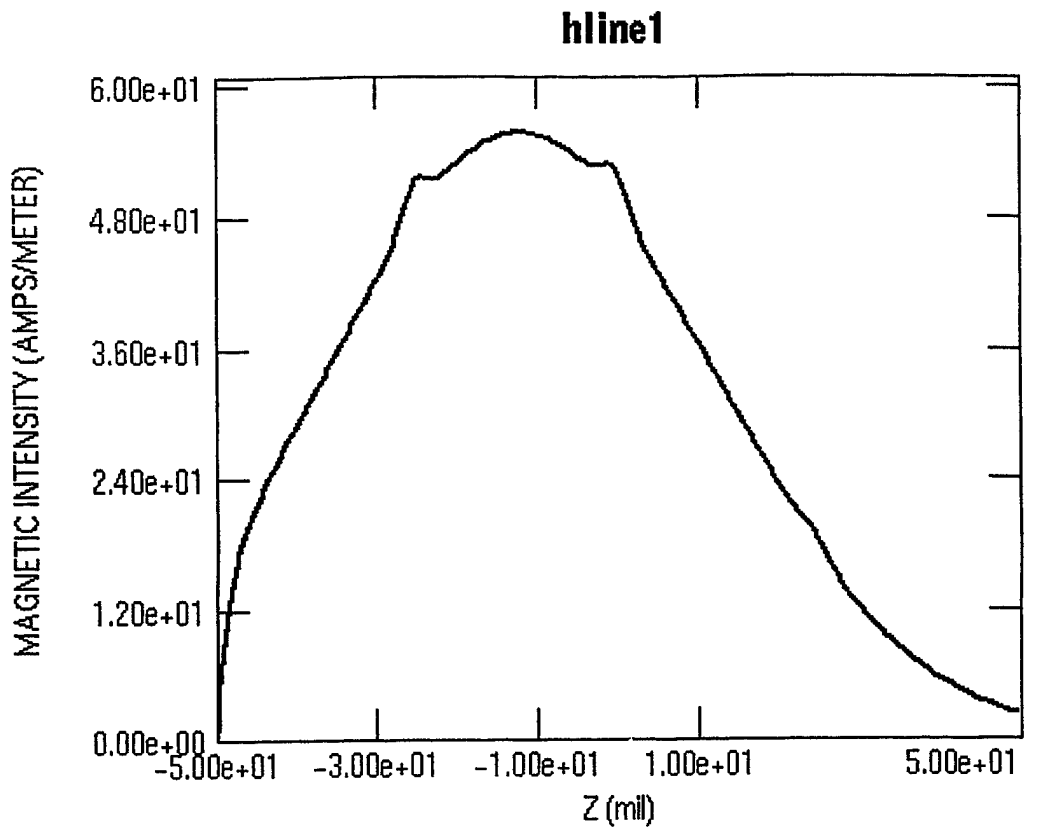


Fig. 4 Current density distributions at the time of maximum coupling from the signal trace (Line 1) to the first crossing trace (Line 2). Top: variation of H_z (equivalently, J_z) with z along the signal trace. Bottom: variation of H_z (equivalently, J_z) with x along the first crossing trace, where $x = 0$ is just above the center line of the signal trace.

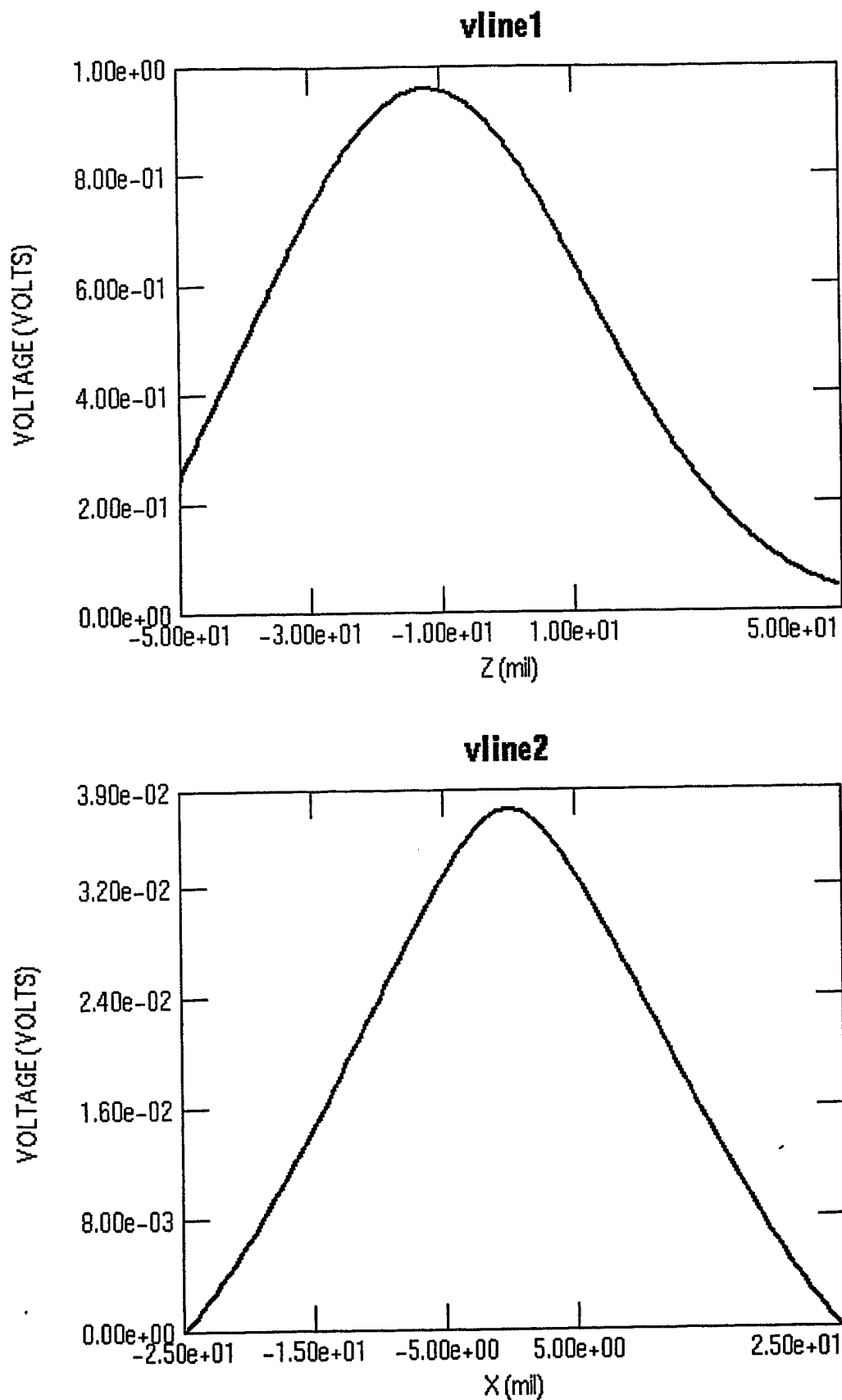


Fig. 5 Potential distributions at the time of maximum coupling from the signal trace (Line 1) to the first crossing trace (Line 2). Top: variation of potential with z along the signal trace. Bottom: variation of potential with x along the first crossing trace, where $x = 0$ is just above the center line of the signal trace. All potentials are referenced to the lower ground plane.

4.3 Example 3: Arcing Between Circuit Traces Carrying High RF Power

This example involves the detailed 3-D FD-TD modeling of an 837-MHz resonant RF power combiner constructed of a single-layer ceramic circuit board. Field reports indicated that this device is susceptible to arcing and scorching, but this failure mode is sporadic and unpredictable.

The power combiner consists of an S-shaped stripline laid down on a 1.524-mm (60-mils) thick alumina substrate over ground having the dielectric parameters $\epsilon_r = 9.8$ and $\tan \delta = 0.0001$. The combiner has six straight stripline sections laid out at right angles. Stripline lengths are as follows:

Trace 1.	36.068 mm (1420 mils)	z-directed;	connected to a 50-ohm RF power source.
Trace 2.	8.128 mm (320 mils)	x-directed	
Trace 3.	19.304 mm (760 mils)	z-directed;	designated the "center trace."
Trace 4.	8.128 mm (320 mils)	x-directed;	designated the "top trace."
Trace 5.	20.828 mm (820 mils)	z directed	
Trace 6.	13.208 mm (520 mils)	x-directed;	ends with a 50-ohm load to ground.

To adjust the operation of the combiner, a 15.24 x 20.32 x 2.032-mm (600 x 800 x 80-mils) barium titanate "puck" having the dielectric parameters $\epsilon_r = 37$ and $\tan \delta = 0.0001$ rests on the surface of the circuit board so that it partially covers the S-shape. A field technician adjusts the position of this ceramic puck to vary the partial overlap, thereby tuning the resonance of the combiner. It was found that arcing is most likely when the left edge of the puck is located 0.508 mm (20 mils) to the right of the center trace, and the top edge of the puck is located 2.032 mm (80 mils) beyond the top trace. By observing the scorch marks on the surface of the alumina substrate, it was determined that the arcing originates at the junction of the center and top traces (Traces 3 and 4, respectively) and burrows under the barium titanate puck in the +x-direction towards Trace 1.

The FD-TD model uses a uniform space increment of 0.508 mm (20 mils) and a time step of 0.8467 ps. Fig. 6 is a color visualization of the FD-TD-computed amplitude of the sinusoidal steady-state E_x field distribution at the surface of the alumina substrate. E_x was selected for visualization since the arcing was observed to occur in the x-direction. Note that the position of the barium titanate puck is visible as a weak rectangular shadow in this figure. From the color coding, where white denotes maximum field amplitude, we see that the FD-TD model predicts that the maximum E_x field arises at the junction of the center and top traces, exactly where arcing was experienced in practice. In fact, elevated E_x fields are seen to arise all along the gap between the center trace and the left side of the puck. Further, scaling of the computed peak E_x intensities to the normal operating power of the combiner shows electric field levels nearly at the breakdown threshold of air at standard temperature, pressure, and humidity. This helps to explain the erratic nature of the observed arcing, since:

1. The combiners were not hermetically sealed, and the variability of normal atmospheric conditions could shift the breakdown threshold of the air inside the combiner.
2. Slight differences in the manual adjustment of the puck position by various field technicians at various sites could slightly increase or decrease the peak electric field, thereby causing the combiner to be respectively closer to, or further from, breakdown.

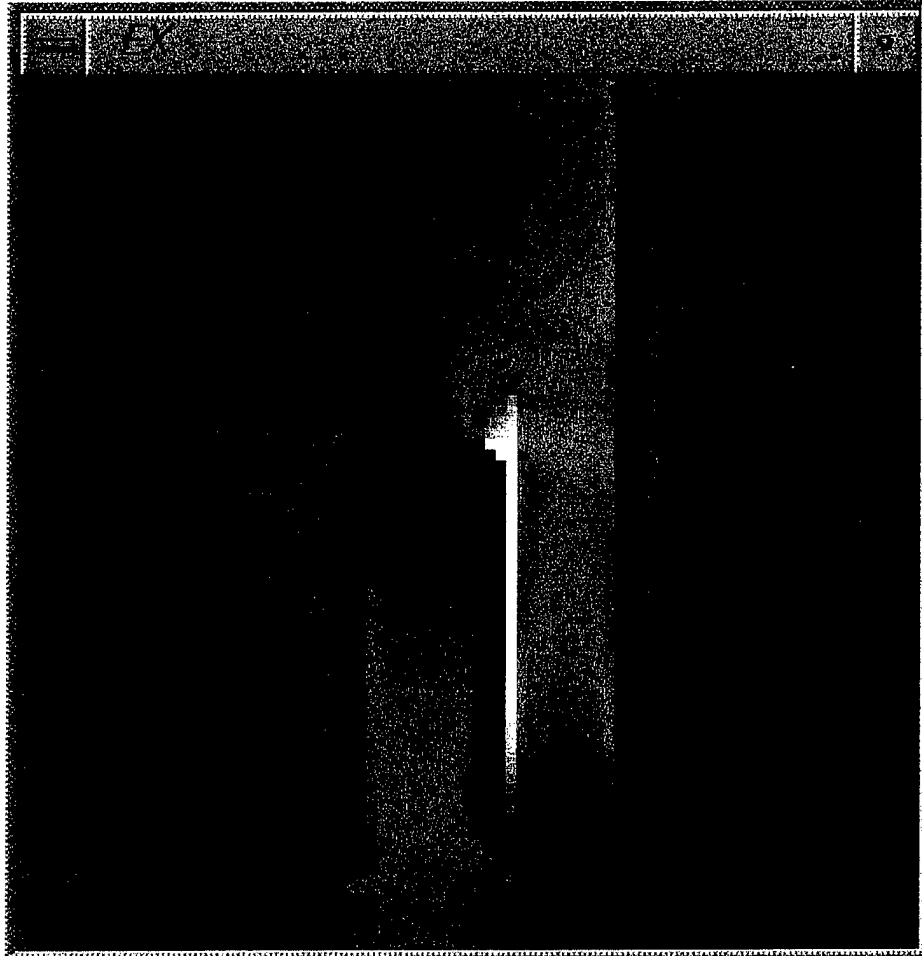


Fig. 6 Visualization of the FD-TD-computed amplitude of the sinusoidal steady-state E_x field distribution at the surface of the alumina substrate of the RF power combiner at 837 MHz. Color scale: decreasing intensity from white to yellow to red to purple to black. Note that the position of the barium titanate puck is visible as a weak rectangular shadow having its left edge just to the right of the center trace.

5.0 TASK 3. PROCEED WITH FD-TD/SPICE SOFTWARE DEVELOPMENT

5.1 Introduction

This section reports the continuation of the development of a hybrid software combining FD-TD field analysis and SPICE nonlinear circuit analysis. This work should eventually permit full-wave simulation of high-speed digital modules, including both the operation of the active logic devices and the passive interconnects between these devices.

Reference [30] demonstrated that it is possible to construct local software links between the three-dimensional FD-TD Maxwell's equations software and appropriate SPICE kernels. This software forms an interface between the time-stepping of the linear, distributed, full-vector electromagnetic (\vec{E} , \vec{H}) fields and the nonlinear, lumped, scalar voltages and currents (V , I) of arbitrarily complex electronic circuits (such as gate arrays) that have negligible electromagnetic wave propagation effects within the circuit. Effectively, the SPICE link permits FD-TD subgrid models of transistors, logic gates, and gate arrays to be constructed that incorporate all important aspects of their circuit physics, including nonlinearities at inputs and outputs, device parasitics, and time delays and/or input/output logic-state shifts due to analog or digital operations occurring within the device.

5.2 Formulation

The connection between Maxwell's equations and SPICE is simple and elegant. The approach is suitable for modeling an arbitrary two-port active network in the context of the time-varying electromagnetic field. With the hybrid FD-TD/SPICE method, the network is replaced with equivalent current sources at the location of its two ports in the space grid. At each port, the equivalent sources must satisfy the possibly nonlinear current-voltage relationship of the network and provide the same response as the network when an electromagnetic wave arrives.

We now summarize the basis of defining the equivalent sources. Consider the differential form of Ampere's Law written at the location of a single, pointwise-connected circuit element:

$$\epsilon \frac{\partial \vec{E}}{\partial t} + \vec{J}(\vec{E}) = \nabla \times \vec{H} \quad (33)$$

Here, the first term on the left-hand side is the local displacement current density. The second term on the left-hand side is the conduction current density due to the circuit element. In general, the conduction current density can have a nonlinear dependence upon the local \vec{E} . To implement the usual leapfrog FD-TD time-stepping, a time central-difference equation can be obtained from (33) by treating it as an ordinary differential equation in time with the right-hand side assumed to be a constant value established at the midpoint of the time step. Note that this procedure keeps the time dependence for $\vec{J}(\vec{E})$. As shown in [3], the resulting differential equation can be accurately time-stepped for a variety of single circuit elements (the resistor, capacitor, inductor, and diode).

However, for the case of one of the ports of an arbitrary two-port nonlinear active circuit connected to the observation point, \vec{J} would be a function of the action of all of the linear and nonlinear devices comprising the circuit, as well as both the local \vec{E} and the remote \vec{E} sensed at

the other port of the circuit. In this case, the simple single-element time-stepping approach of [3] would not be useful. A rationale for involving the general circuit simulator SPICE now become apparent. Because SPICE calculates the current through a circuit element as a function of the voltage across the device, SPICE could provide $\vec{J}(\vec{E})$ for a circuit device simultaneously exposed to the electromagnetic field and embedded in a general electrical network. This value of \vec{J} could be used in the left-hand side of (33), and a separate time central-difference procedure could be done to provide the time-stepping relation for \vec{E} .

However, an even simpler and more robust solution [30] can be obtained by rewriting (33) as

$$C_{\text{grid cell}} \frac{dV_{\text{device}}}{dt} + I_{\text{device}}(V_{\text{device}}) = I_{\text{total}} \quad (34)$$

where

V_{device} is the voltage across the circuit device, and therefore, the grid cell;

$C_{\text{grid cell}} = \epsilon A / \Delta$ is the FD-TD grid-cell capacitance, where A is the cross-section area of the grid cell and Δ is its height;

$I_{\text{device}}(V_{\text{device}}) = A J(E)$ is the current flowing through the device, which can have a nonlinear dependence upon V_{device} ; and

I_{total} is the known total current flowing through the grid cell, which equals the line integral of the H-field vector components looping around the cell. These H components were just obtained in the magnetic field time-stepping part of the FD-TD algorithm.

Equation (34) can be represented as an equivalent circuit consisting of a current source in parallel with a capacitor. Thus, instead of using SPICE just to determine $J(E)$, SPICE can be used to time-step (34) *directly* to update V_{device} , which then yields the desired updated cell electric field by the simple relation $E = V_{\text{device}} / \Delta$. In this way, the lumped element can be an arbitrarily large SPICE network whose description can be contained in a standard SPICE file. Furthermore, all of the extensive device models in SPICE can be used directly in the FD-TD simulation without the need to duplicate the model development; and the efficient circuit integration methods used in SPICE are also directly available without user-implemented integration schemes.

5.3 Reported Applications

This approach was successfully implemented in [30]. Initial comparisons were made between FD-TD/SPICE and pure SPICE simulations for one-port circuits placed at the end of a microstrip line. These included individual resistors, capacitors, inductors, and diodes, and then progressed to more complicated multi-element circuits consisting of several series and parallel components. All FD-TD data were in excellent agreement with the appropriate pure SPICE model.

Reference [30] then reported the modeling of a more interesting nonlinear two-port network, a VHF tuned amplifier mounted on a circuit board. The overall circuit consisted of a step-

function voltage source, a source microstrip line, an NPN bipolar junction transistor embedded with LC networks for base and collector impedance matching, a load microstrip line, and a resistive load. Excellent agreement on the order of 1% was obtained between the FD-TD/SPICE results for the complicated transistor base-voltage time waveform and a pure SPICE model that was constructed to account for the physics of the two transmission lines. Similar agreement was observed for the collector voltage waveform. This high level of agreement indicated that the FD-TD/SPICE model permitted a self-consistent simulation of the flow of electromagnetic wave energy in both directions through the nonlinear two-port amplifier network.

Reference [31] reported the use of FD-TD/SPICE to perform a small-signal analysis of a 5.7-GHz center-frequency microwave amplifier consisting of a three-terminal packaged FET, its biasing circuit, the associated resistors and capacitors, and the strip line interconnects. Using a modulated Gaussian pulse excitation, the S -parameters were obtained over a wide frequency range using the discrete Fourier transform of the calculated time responses, as discussed earlier. Solid agreement was obtained between the calculated and measured S -parameters over the range dc to 9 GHz. In further work by this group, a power amplifier was analyzed for large-signal excitation. The results were in good agreement with those of the harmonic balance analysis [32].

5.4 Potential Applications

The hybrid FD-TD/SPICE tool will be optimally applied when the speed of a circuit is so high and its physical embedding is so complex that modeling electro-magnetic wave "artifacts" is crucial. Both digital and analog applications are expected:

1. *Digital*. An increasingly wide range of digital applications is expected as clock speeds approach microwave frequencies. Present engineering practice of using electromagnetic field solvers only to obtain lumped-circuit equivalences for subsequent insertion into conventional SPICE models may one day yield to *direct time-domain modeling* of logic operations from FD-TD/SPICE.
2. *Analog*. Here applications will include analysis of linearity, intermodulation, harmonic generation, and conversion efficiency of MMICs embedded in compact and complex structures. Another category of applications will include radiation, especially by arrays of surface patch antennas excited by Gunn diodes, tunnel diodes, transistor oscillators, and MMICs located directly at the antenna [33].

FD-TD/SPICE should also have excellent applicability to modeling digital or analog circuit upset due to external natural and manmade electromagnetic insults such as lightning, electromagnetic pulse, and high-power microwaves.

REFERENCES

- [1] Zhang, X., and K. K. Mei, "Time-domain finite-difference approach for the calculation of the frequency-dependent characteristics of microstrip discontinuities," *IEEE Trans. Microwave Theory and Techniques*, vol. 36, 1988, pp. 1775-1787.
- [2] Fang, J. and D. Xue, "Numerical errors in the computation of impedances by FDTD method and ways to eliminate them," *IEEE Microwave and Guided Wave Letters*, vol. 5, 1995, pp. 6-8. See also comments on this paper in *IEEE Microwave and Guided Wave Letters*, vol. 5, 1995, pp. 354-355.

- [3] Piket-May, M. J., A. Taflove, and J. Baron, "FD-TD modeling of digital signal propagation in 3-D circuits with passive and active loads," *IEEE Trans. Microwave Theory and Techniques*, vol. 42, 1994, pp. 1514-1523.
- [4] Ramo, S., J. R. Whinnery, and T. Van Duzer, *Fields and Waves in Communications Electronics*, 2nd ed., New York: Wiley, 1984.
- [5] Sheen, D. M., S. M. Ali, M. D. Abouzahra, and J. A. Kong, "Application of the three-dimensional finite-difference time-domain method to the analysis of planar microstrip circuits," *IEEE Trans. Microwave Theory and Techniques*, vol. 38, 1990, pp. 849-857.
- [6] Yook, J.-G., N. I. Dib, and L. P. B. Katehi, "Characterization of high-frequency interconnects using finite difference time domain and finite element methods," *IEEE Trans. Microwave Theory and Techniques*, vol. 42, 1994, pp. 1727-1736.
- [7] Becker, W. D., P. H. Harms, and R. Mittra, "Time-domain electromagnetic analysis of interconnects in a computer chip package," *IEEE Trans. Microwave Theory and Techniques*, vol. 40, 1992, pp. 2155-2163.
- [8] Harms, P., J. Lee, and R. Mittra, "Characterizing the cylindrical via discontinuity," *IEEE Trans. Microwave Theory and Techniques*, vol. 41, 1993, pp. 153-156.
- [9] Mittra, R., S. Chebolu, and W. D. Becker, "Efficient modeling of power planes in computer packages using the finite difference time domain method," *IEEE Trans. Microwave Theory and Techniques*, vol. 42, 1994, pp. 1791-1795.
- [10] Hildebrand, F. B., *Introduction to Numerical Analysis*, New York: Dover, 1974, pp. 457-462.
- [11] Dubard, J. L., D. Pompei, J. Le Roux, and A. Papiernik, "Characterization of microstrip antennas using the TLM simulation associated with a Prony-Pisrenko method," *Int. J. Numerical Modeling*, vol. 3, 1990, pp. 269-285.
- [12] Ko, W. L., and R. Mittra, "A combination of FD-TD and Prony's methods for analyzing microwave integrated circuits," *IEEE Trans. Microwave Theory and Techniques*, vol. 39, 1991, pp. 2176-2181.
- [13] Pereda, J. A., L. A. Vielva, and A. Prieto, "Computation of resonant frequencies and quality factors of open dielectric resonators by a combination of the finite-difference time-domain (FDTD) and Prony's methods," *IEEE Microwave and Guided Wave Letters*, vol. 2, 1992, pp. 431-433.
- [14] Maloney, J. G., and G. S. Smith, "The use of surface impedance concepts in the finite-difference time-domain method," *IEEE Trans. Antennas and Propagation*, vol. 40, 1992, pp. 38-48.
- [15] Kumaresan, R., and D. W. Tufts, "Estimating the parameters of exponentially damped sinusoids and pole-zero modeling in noise," *IEEE Trans. Acoustics, Speech, and Signal Processing*, vol. 30, 1982, pp. 833-840.
- [16] Kay, S. M., and S. L. Marple, "Spectrum analysis- a modern perspective," *Proc. IEEE*, vol. 69, 1981, pp. 1380-1419.
- [17] Chen, J., C. Wu, T. K. Y. Lo, K.-L. Wu, and J. Litva, "Using linear and nonlinear predictors to improve the computational efficiency of the FD-TD algorithm," *IEEE Trans. Microwave Theory and Techniques*, vol. 42, 1994, pp. 1992-1997.
- [18] Kay, S. M., *Modern Spectral Estimation*, Englewood Cliffs, NJ: Prentice-Hall, 1988.
- [19] Ulrych, T. J., and R. W. Clayton, "Time series modeling and maximum entropy," *Phys. Earth and Plan. Int.*, vol. 12, 1976, pp. 188-200.
- [20] Nuttall, A. H., "Spectral analysis of a univariate process with bad data points via maximum entropy and linear predictive techniques," Naval Underwater Systems Center, New London, CT, Tech. Report 5303, March 26, 1976.
- [21] Marple, L., "A new autoregressive spectrum analysis algorithm," *IEEE Trans. Acoustics, Speech, and Signal Processing*, vol. 28, 1980, pp. 441-454.
- [22] Jandhyala, V., E. Michielssen, and R. Mittra, "FDTD signal extrapolation using the forward-backward autoregressive (AR) model," *IEEE Microwave and Guided Wave Letters*, vol. 4, 1994, pp. 163-165.
- [23] Haggan, V., and T. Ozaki, "Modeling nonlinear random vibrations using an amplitude-dependent autoregressive time series model," *Biometrika*, vol. 68, 1981, pp. 189-196.

- [24] Tong, H., *Non-Linear Time Series*, Cambridge, U.K.: Oxford University Press, 1990.
- [25] Goodwin, G. C., and K. S. Sin, *Adaptive Filtering Prediction and Control*, Englewood Cliffs, NJ: Prentice-Hall, 1984.
- [26] Kuempel, W., and I. Wolff, "Digital signal processing of time-domain field simulation results using the system identification method," *IEEE MTT-S Int. Microwave Symposium Digest*, vol. 2, 1992, pp. 793-796.
- [27] Houshmand, B., T. W. Huang, and T. Itoh, "Microwave structure characterization by a combination of FDTD and system identification methods," *IEEE Microwave and Guided Wave Letters*, vol. 3, 1993, pp. 262-264.
- [28] Huang, T.-W., B. Houshmand, and T. Itoh, "Fast sequential FDTD diakoptics method using the system identification technique," *IEEE Microwave and Guided Wave Letters*, vol. 3, 1993, pp. 378-380.
- [29] Huang, T.-W., B. Houshmand, and T. Itoh, "The implementation of time-domain diakoptics in the FDTD method," *IEEE Trans. Microwave Theory and Techniques*, vol. 42, 1994, pp. 2149-2155.
- [30] Thomas, V. A., M. E. Jones, M. J. Picket-May, A. Taflove, and E. Harrigan, "The use of SPICE lumped circuits as sub-grid models for FD-TD high-speed electronic circuit design," *IEEE Microwave and Guided Wave Letters*, vol. 4, 1994, pp. 141-143.
- [31] Kuo, C.-N., R.-B. Wu, B. Houshmand, and T. Itoh, "Modeling of microwave active devices using the FDTD analysis based on the voltage-source approach," *IEEE Microwave and Guided Wave Letters*, in press.
- [32] Kuo, C.-N., B. Houshmand, and T. Itoh, "Large-signal analysis of a microwave amplifier using FDTD method," submitted to *1996 IEEE MTT-S International Microwave Symposium*
- [33] Thomas, V. A., K.-M. Ling, M. E. Jones, B. Toland, J. Lin, and T. Itoh, "FDTD analysis of an active antenna," *IEEE Microwave and Guided Wave Letters*, vol. 4, 1994, pp. 296-298.

***MISSION
OF
AFRL/INFORMATION DIRECTORATE (IF)***

The advancement and application of information systems science and technology for aerospace command and control and its transition to air, space, and ground systems to meet customer needs in the areas of Global Awareness, Dynamic Planning and Execution, and Global Information Exchange is the focus of this AFRL organization. The directorate's areas of investigation include a broad spectrum of information and fusion, communication, collaborative environment and modeling and simulation, defensive information warfare, and intelligent information systems technologies.